

Radio and γ -ray activity in the jet of the blazar S5 0716+714

DAE-WON KIM,^{1,2} EVGENIYA V. KRAVCHENKO,^{3,4,5} ALEXANDER M. KUTKIN,^{6,4} MARKUS BÖTTCHER,⁷ JOSÉ L. GÓMEZ,⁸ MARK GURWELL,⁹ SVETLANA G. JORSTAD,^{10,11} ANNE LÄHTEENMÄKI,^{12,13} ALAN P. MARSCHER,¹⁰ VENKATESH RAMAKRISHNAN,¹⁴ MERJA TORNIKOSKI,¹² SASCHA TRIPPE,^{1,15} ZACHARY WEAVER,¹⁰ AND KAREN E. WILLIAMSON¹⁰

¹*Department of Physics and Astronomy, Seoul National University, Gwanak-gu, Seoul 08826, Korea; dwkimastro@gmail.com*

²*Max-Planck-Institut für Radioastronomie, Auf dem Hügel 69, D-53121, Bonn, Germany*

³*Moscow Institute of Physics and Technology, Institutsky per. 9, Moscow region, Dolgoprudny, 141700, Russia*

⁴*Astro Space Center, Lebedev Physical Institute, Russian Academy of Sciences, Profsovnaya st., 84/32, Moscow, 117997, Russia*

⁵*INAF Istituto di Radioastronomia, Via P. Gobetti, 101, Bologna, 40129, Italy*

⁶*ASTRON, Netherlands Institute for Radio Astronomy, Oude Hoogeveensedijk 4, 7991PD, Dwingeloo, The Netherlands*

⁷*Centre for Space Research, North-West University, Potchefstroom, 2520, South Africa*

⁸*Instituto de Astrofísica de Andalucía, CSIC, Glorieta de la Astronomía s/n, Granada, 18008, Spain*

⁹*Center for Astrophysics | Harvard & Smithsonian, 60 Garden Street, Cambridge, MA 02138, USA*

¹⁰*Institute for Astrophysical Research, Boston University, 725 Commonwealth Avenue, Boston, MA 02215, USA*

¹¹*Astronomical Institute, St. Petersburg State University, Universitetskij Pr. 28, Petrodvorets, 198504 St. Petersburg, Russia*

¹²*Aalto University Metsähovi Radio Observatory, Metsähovintie 114, FI-02540 Kylmälä, Finland*

¹³*Aalto University Department of Electronic and Nanoengineering, PL15500, FI-00076 Aalto, Finland*

¹⁴*Astronomy Department, Universidad de Concepción, Casilla 160-C, 4030000 Concepción, Chile*

¹⁵*SNU Astronomy Research Center, Seoul National University, 1 Gwanak-ro, Gwanak-gu, Seoul 08826, Korea*

(Received 27 February 2021; Revised 30 September 2021; Accepted 19 October 2021)

Submitted to ApJ

ABSTRACT

We explore the connection between the γ -ray and radio emission in the jet of the blazar 0716+714 by using 15, 37, and 230 GHz radio and 0.1–200 GeV γ -ray light curves spanning 10.5 years (2008–2019). We find significant positive and negative correlations between radio and γ -ray fluxes in different time ranges. The time delays between radio and γ -ray emission suggest that the observed γ -ray flares originated from multiple regions upstream of the radio core, within a few parsecs from the central engine. Using time-resolved 43 GHz VLBA maps we identified 14 jet components moving downstream along the jet. Their apparent speeds range from 6 to 26 c , showing notable variations in their position angles upstream the stationary component (~ 0.53 mas from the core). The brightness temperature declines as function of distance from the core according to a power-law which becomes shallower at the location of the stationary component. We also find that the periods at which significant correlations between radio and γ -ray emission occur overlap with the times when the jet was oriented to the north. Our results indicate that the passage of a propagating disturbance (or shock) through the radio core and the orientation of the jet might be responsible for the observed correlation between the radio and γ -ray variability. We present a scenario that connects the positive correlation and the unusual anti-correlation by combining the production of a flare and a dip at γ -rays by a strong moving shock at different distances from the jet apex.

Keywords: Galaxies: active – BL Lacertae objects: individual: 0716+714 – Galaxies: jets – Gamma rays: galaxies

1. INTRODUCTION

Blazars (Angel & Stockman 1980) are a class of active galactic nuclei (AGN) that show extreme variability on various timescales (e.g. Bhatta et al. 2013). It is widely believed that they are powered by accretion onto supermassive black holes, accompanied by the formation of two-sided relativis-

tic outflows or jets. Due to their preferential orientation close to the line of sight ($\lesssim 5^\circ$, Hovatta et al. 2009a; Jorstad et al. 2017; Liodakis et al. 2018a), blazar jet components exhibit superluminal speeds up to a few tens of the speed of light (e.g., Liodakis et al. 2018a), as well as significant enhancement of their emission due to Doppler boosting. The vast

majority of sources detected by the Large Area Telescope (LAT) on board the *Fermi Gamma-ray Space Telescope* in the GeV band are blazars (Abdo et al. 2010a). Detection of a significant correlation between the radio flux density and γ -ray flux (Kovalev et al. 2009; Pushkarev et al. 2010; Fuhrmann et al. 2014) indicates a common emission mechanism. The common view is that the jet radio emission is produced by synchrotron radiation from electrons, while the high energy emission can either be generated through inverse Compton scattering (IC) of seed photons by the same electrons (e.g. Sikora et al. 1994) or by hadronic processes (e.g. Mannheim 1998). Most likely, the bulk of the γ -ray emission is produced within the parsec-scale jet (Ramakrishnan et al. 2014; Kravchenko et al. 2016; Lisakov et al. 2017; Kim et al. 2018) and may be associated with stationary structures (e.g. Pushkarev et al. 2019; Kim et al. 2020).

S5 0716+714 (hereafter 0716+714) is one of the most active BL Lacertae objects and also shows intra-day variability (e.g. Liao et al. 2014). An early high angular resolution study performed with the Very Long Baseline Interferometry Space Observatory Program in 2000 (VSOP, Bach et al. 2006) located the short term variability of the blazar within $100 \mu\text{as}$ from the radio core (surface of the optical depth $\tau_\nu \sim 1$). Later, on 2015 January 3–4, 0716+714 was observed by the *RadioAstron* space VLBI mission (Kardashev et al. 2013). These observations, conducted at 22 GHz (Kravchenko et al. 2020), revealed complex structure within the innermost $100 \mu\text{as}$ of the jet: a core size of $\leq 8 \mu\text{as}$ extended toward the southeast with limits of $< 12 \times 5 \mu\text{as}$ along the major and minor beam axis, respectively, and a change of the jet position angle by about 95° toward the northeast. A compact linearly polarized component that might be associated with the stationary feature which is considered to be a recollimation shock, is located at a position of $58 \mu\text{as}$ downstream from the core (Rani et al. 2015; Jorstad et al. 2017).

Observations constrain the 0716+714 jet viewing angle to $\leq 5^\circ$ (Bach et al. 2005; Hovatta et al. 2009b; Jorstad et al. 2017), and a stacked-epoch analysis showed that the intrinsic opening angle of the outflow is about 2° (Pushkarev et al. 2017). Alongside the significant curvature in the innermost $100 \mu\text{as}$ (Kravchenko et al. 2020), this suggests that the jet has been viewed at an angle smaller than the opening angle itself, meaning the line of sight is located inside the outflow.

Analysis of the correlation between light curves obtained at different wavelengths is crucial to explore the physics of the long-term flux variations, especially the radiative processes and the location of the emission region (e.g., Lioudakis et al. 2018b). Previous studies of 0716+714 revealed a tight correlation between optical and γ -ray fluxes (Larionov et al. 2013; Rani et al. 2013; Ramakrishnan et al. 2016). Variability of the emission in 0716+714 at these frequencies usually occurs contemporaneously; this supports leptonic emission

models (Mastichiadis & Kirk 1997; Li & Kusunose 2000; Böttcher & Chiang 2002). The connection becomes much more complicated when comparing γ -ray and radio emission. On the one hand, it has been reported that the γ -ray flux shows no significant correlation with the radio emission (Max-Moerbeck et al. 2014b; Ramakrishnan et al. 2015). On the other hand, Rani et al. (2013, 2014) reported not only significant correlations, but also anti-correlated behavior. Butuzova (2018) explains these changes from positive to negative correlations with a helical jet model of 0716+714, where emission observed at different wavelengths originates from spatially separate regions and at different fixed distances from the jet base. Moreover, different mechanisms might be responsible for the generation of high-energy emission at different locations along the jet. Furthermore, as Ramakrishnan et al. (2015) noted, the rapid variability of 0716+714 complicates correlation studies of light curves observed in different frequency bands. In this paper, we further investigate the radio and γ -ray emission of 0716+714 and to pinpoint their production sites in the jet.

0716+714 has no spectroscopic redshift measurement because of its featureless optical continuum and bright optical nucleus. Here we adopt the value of $z = 0.31 \pm 0.08$, derived from the photometric detection of the blazar host galaxy (Nilsson et al. 2008), which is compatible with other estimates (Danforth et al. 2013; MAGIC Collaboration et al. 2018). Throughout the paper, we assume a flat Λ CDM cosmology with a matter density parameter $\Omega_m = 0.3$, cosmological constant parameter $\Omega_\Lambda = 0.7$, and Hubble constant $H_0 = 70 \text{ km s}^{-1} \text{ Mpc}^{-1}$, (Bennett et al. 2014; Planck Collaboration et al. 2016). This corresponds to a luminosity distance D_L of 1.6 Gpc and a scale of 4.56 pc/mas at a redshift of 0.31.

2. OBSERVATIONS

2.1. 15, 37, and 43 GHz data

15 GHz and 37 GHz continuum single-dish monitoring data were obtained from the Owens Valley Radio Observatory¹ (OVRO) and Metsähovi Radio Observatory² operated by Aalto University in Finland, respectively. 0716+714 is one of the target sources in their AGN monitoring programs. A detailed description of the observations and data calibration can be found in Richards et al. (2011) for OVRO data and Teräsranta et al. (1998) for Metsähovi data.

Interferometric multi-epoch observations were obtained through the VLBA-BU-BLAZAR (BU) monitoring program³ at 43 GHz. This program observes ~ 33 γ -ray bright blazars monthly with the Very Long Baseline Array (VLBA).

¹ <https://sites.astro.caltech.edu/ovroblazars/data.php>

² <http://www.metsahovi.fi/AGN/data/>

³ <https://www.bu.edu/blazars/index.html>

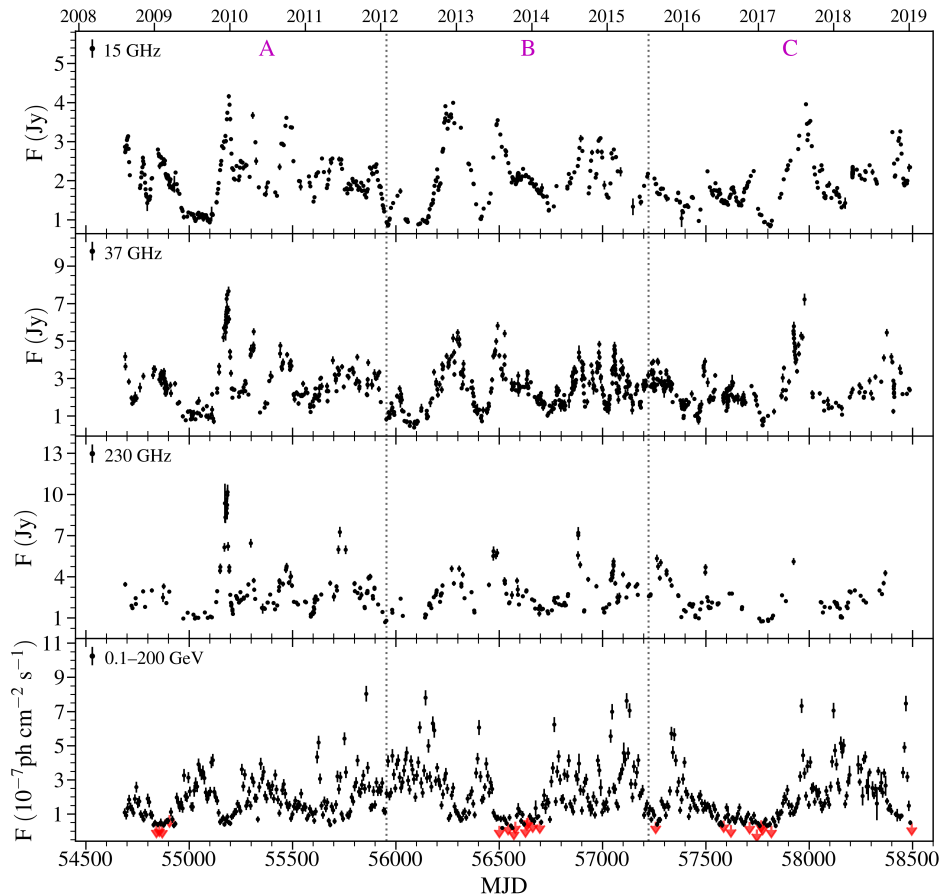


Figure 1. From top to bottom: light curves of the blazar 0716+714 at radio (15, 37 and 230 GHz) and γ -ray (0.1–200 GeV) bands. The γ -ray light curve was binned to one value per week, the red arrows indicate 3σ upper limits. The vertical dashed lines distinguish three 3.5-year long periods (A, B, and C), thus dividing the whole time range into three equal segments (see Section 3.2.1). Observing times are given in years along the top and in MJD along the bottom horizontal axis.

We analyzed 118 BU-epochs in total, which span about 10.5 years (from June 2008 to December 2018). Details of the data calibration are given in (Jorstad et al. 2017).

2.2. SMA 230 GHz (1.3 mm)

The 230 GHz (1.3 mm) flux density data were obtained at the Submillimeter Array (SMA) on Mauna Kea (Hawaii). 0716+714 is included in an ongoing monitoring program at the SMA which monitors the fluxes of compact extragalactic radio sources that can be used as calibrators at mm wavelengths (Gurwell et al. 2007). Potential calibrators are occasionally observed for 3 to 5 minutes, and the measured source signal strength is calibrated against known standards, typically solar system objects (Titan, Uranus, Neptune, or Callisto). Data from this program are updated regularly and are available at the SMA website⁴.

2.3. γ -ray flux

We obtained γ -ray fluxes in the energy range 0.1–200 GeV from observations by the *Fermi*-LAT, by compiling data from 2008 through the beginning of 2019. The analysis was done using the *Fermi* Science Tools software package⁵ version v10r0p5 and Pass 8 data, including the instrument response functions `gll_iem_v07` and the `iso_P8R3_SOURCE_V2_v1` diffuse source models. Photons were selected within a 15° radius centered on the source, using the `gtselect` tool with `evclass` of 128, `evtype` of 3 and maximum zenith angle of 90° . Sources from the 4FGL catalog (Acero et al. 2015) with high test statistic values ($TS \geq 25$, Mattox et al. 1996) were used to generate the background source model. The emission from 0716+714 was modelled assuming a log-parabolic photon spectrum ($dN/dE = N_0(E/E_b)^{-(\alpha+\beta \log(E/E_b))}$, where $E_b = 428.655$ MeV, $\alpha=2.01$ and $\beta=0.0375$). We produced a light curve binned into weekly intervals. For each time bin, the integrated flux values were computed using the maximum-likelihood algorithm implemented in the science tool `gtlike`

⁴ <http://sma1.sma.hawaii.edu/callist/callist.html>

⁵ <http://fermi.gsfc.nasa.gov/ssc/>

to estimate the significance of a detection. We used a detection criterion which corresponds to a maximum-likelihood test statistic $TS > 10$ (Abdo et al. 2011a). If no significant flux was detected, we computed a 3σ upper limit. More details on the γ -ray data reduction can be found in Williamson et al. (2014).

3. RESULTS

3.1. Radio and γ -ray light curves

Figure 1 shows the OVRO (15 GHz), Metsähovi (37 GHz), SMA (230 GHz), and LAT (0.1–200 GeV) light curves of 0716+714 from MJD 54687 to MJD 58490 (August 2008 to January 2019). 0716+714 is highly variable at all bands, while the average flux density and variability become stronger and faster at shorter wavelengths. The radio light curves were sampled at irregular intervals, the average sampling intervals are ~ 6 , 5, and 12 days at 15, 37, and 230 GHz, respectively. From the weekly γ -ray light curve, two distinct groups of flaring states can be distinguished. First, there are three minor, short-term (on scales of months) flares in an otherwise quiescent period until 2011 (see the top and bottom time axes in Figure 1). Afterwards, three major, long-term (on scales of years) flares can be seen in 2011–2013, 2014–2016, and 2017–2019, respectively. The radio light curves show frequent flaring: there are roughly 20–30 individual events throughout our observations, with an average duration of a radio flare of about one month. This is untypical for blazars, which usually show characteristic radio variability time scales of on the order of years (e.g., Hovatta et al. 2007; Trippe et al. 2011).

3.2. Correlation analysis

3.2.1. Long-term γ -ray–37 GHz correlation

We search for correlations between the observed radio and γ -ray light curves over the entire observing time range using the discrete cross-correlation function (DCF; Edelson & Krolik 1988). We computed confidence levels for DCF curves by simulating γ -ray light curves in the manner of Emmanoulopoulos et al. (2013). In order to obtain input parameters for the simulation, we calculated a periodogram and measured the power-law slope of the spectral density (powerlaw spectral density, PSD) which follows $PSD \propto 1/\nu^\beta$. We also calculated the probability density function (PDF) of the γ -ray light curve, using log-normal and gamma (Γ) functions. To calculate the periodogram of the γ -ray light curve, we linearly interpolated missing flux points (i.e., upper limits); the difference between the upper limits and the resultant fluxes is on average $\pm 0.1 \times 10^{-7}$ ph cm $^{-2}$ s $^{-1}$. For consistency, this interpolated γ -ray light curve was used in the simulation and DCF analysis throughout this study. Bin sizes for DCFs were the larger of the two sampling intervals for any pair of time series.

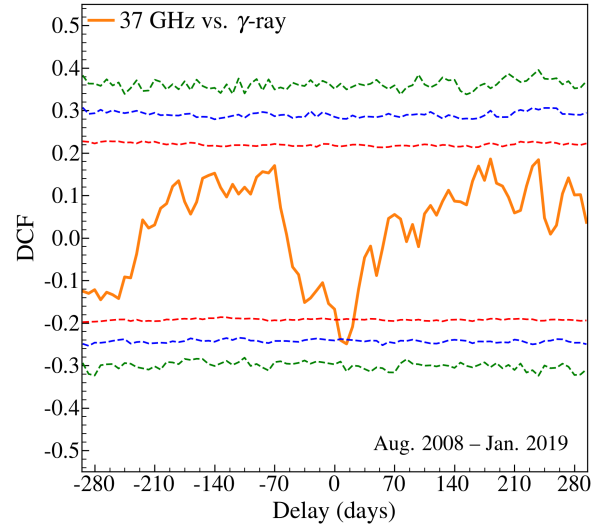


Figure 2. Discrete correlation function (DCF) as function of relative time comparing the 37 GHz and γ -ray light curves over the full 10.5 year observing time range. The red, blue, and green dashed lines denote the 95, 99, and 99.9 % confidence levels, respectively.

We generated 10,000 artificial γ -ray light curves spanning time ranges 10 times longer than the length of the input light curve to minimize the impact of red-noise leakage (Uttley et al. 2002). From each artificial light curve we drew a subsample having the length of the observed light curve and rescaled it to the mean and standard deviation of the input data. We sampled the artificial light curves into time bins spanning one week to match the sampling of the observed γ -ray data. Therefore, we expect that aliasing is negligible (Emmanoulopoulos et al. 2013). Since the DCF coefficient values do not always follow Gaussian distributions, we calculated the cumulative distribution function (CDF) of the DCF coefficients to find the 95, 99, and 99.9% confidence levels (Robertson et al. 2015); these three levels correspond to 2σ , 2.6σ , and 3.3σ , respectively for a normal distribution. Since the DCF coefficient values frequently deviate from a normal distribution, we used the more conservative significance level of 3.3σ ($\sim 99.9\%$) instead of 3σ ($\sim 99.7\%$) as the limit for a significant detection.

First, we investigated the overall radio-to- γ -ray correlation using the 37 GHz radio data owing to their denser sampling and because of non-zero contribution of interstellar scintillation up to 15 GHz (Koay et al. 2019). Figure 2 shows the resultant DCF over the whole observed 10.5-year time range adopting a seven-day binning. We find a significant negative correlation exceeding the 99% confidence level. The minimum DCF value of -0.25 is located at a delay of around 15 days, with the radio leading the γ -ray emission.

To explore the origin of this unusual anticorrelation more deeply, we split the whole observing time range into three

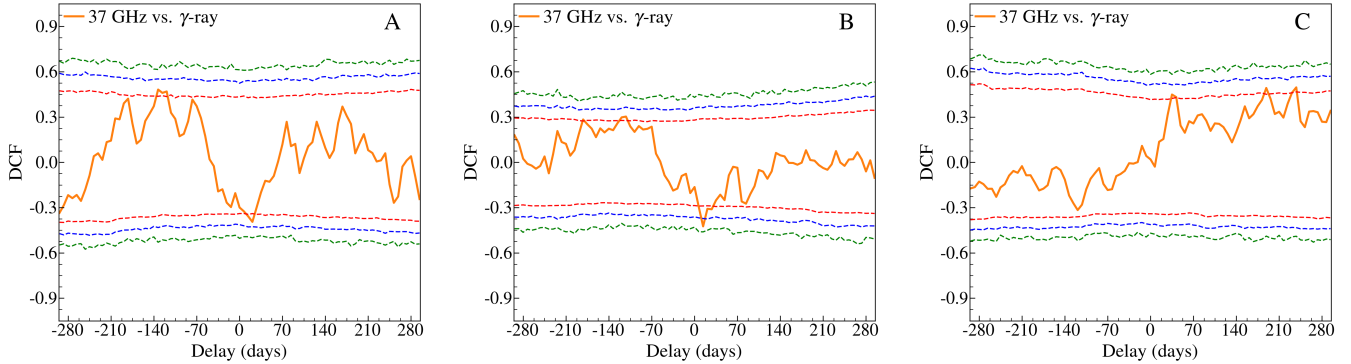


Figure 3. Discrete correlation function (DCF) as function of time delay comparing 37 GHz and γ -ray light curves within three 3.5 yr periods: *A* (MJD 54687–55954.7), *B* (MJD 55954.7–57222.3), and *C* (MJD 57222.3–58490). The red, blue, and green dashed lines denote the 95, 99, and 99.9 % confidence levels, respectively.

equal 3.5-year long intervals: *A* (MJD 54687–55954.7), *B* (MJD 55954.7–57222.3), and *C* (MJD 57222.3–58490). The correlation analysis was performed again within each of these time ranges. The results are shown in Figure 3. In interval *A*, we found two DCF peaks exceeding the 95% confidence levels. A negative correlation was again found at 21 days with a coefficient of -0.39 . In addition, there is a positive correlation at about -125 days with a coefficient of ~ 0.48 . A similar trend can be seen in region *B*. Here, the negative correlation is more significant than the one in *A*, exceeding the 99% confidence level. It is located at 14 days with the coefficient being -0.43 . In addition, positive correlation values exceed the 95% confidence level at two time delays. Given their values and locations, the one located at -112 days with the coefficient of 0.3 appears more probable. In interval *C*, positive correlation values exceed the 95% confidence level at multiple delays. Given the positive delays (i.e., radio-leading) and the relatively sparse sampling of the radio data in this period, these correlation peaks seem to be artifacts (see Section 3.2.2).

Our correlation analysis suggests the presence of both positive and negative significant correlations between the radio and γ -ray light curves in each of the *A* (2008–2012) and *B* (2012–2016) periods, plus a potential positive correlation in *C*. The correlation coefficients are larger in each of the individual intervals than for the entire observing time. This is consistent with rapid variability, including multiple flaring events, weakening any underlying intrinsic correlation. Another natural explanation is a time dependence of the delays, which washes out the correlation if too long time intervals are analyzed.

3.2.2. Optimization of time ranges

We further explored the main source of the significant radio-to- γ -ray correlations by narrowing down the time range. During the correlation analysis for the γ -ray and the unevenly sampled radio light curves, we noted that some of the extended time gaps between radio data points (cor-

responding to empty bins in an evenly sampled light curve) result in spurious DCF peaks. This effect was particularly severe during the *C* period for both the 37 GHz and 230 GHz data. To reduce this effect, we modeled the observed radio light curves using interpolation and Hanning windowing (e.g., Max-Moerbeck et al. 2014a; Ramakrishnan et al. 2016). The model light curves were then sampled into regular bins with durations corresponding to their observed average sampling intervals. Since the radio and γ -ray light curves were sampled differently, we employed the DCF, rather than a simpler direct cross-correlation method, for our analysis.

We analyzed the *A*, *B*, and *C* periods again, using again the 37 GHz light curve as proxy for radio emission in general. For each 3.5-year period, we defined a sliding window shifting from left to right along the time axis. Due to the frequent and short radio flares, DCF peaks decrease considerably with increasing window size (see also Ramakrishnan et al. 2015, for the effects of the rapid variability on the correlation). Hovatta et al. (2008) reported an average AGN flare timescale of one year at 37 GHz. Considering the 27 individual 37 GHz flares identified by Kravchenko et al. (2020), however, the typical flare duration (e.g., Abdo et al. 2010b) of 0716+714 is closer to approximately 4 months (see also Lee et al. 2017, for similar estimates in the source). Furthermore, the jet of 0716+714 is known to frequently eject new radio jet components (about every half year; Jorstad et al. 2017), which coincide with the numerous radio flares shown in Figure 1. Hence, we settled on 1.5 years as a reasonable size for the sliding window.

While the window passes through the 37 GHz and γ -ray light curves in parallel, we generated and stored DCF curves (~ 720 in total) at each time step. We then identified two “extreme” DCF curves in each of the *A/B/C* periods: the one with the highest (positive) and the one with the lowest (most negative) DCF value. If an extremal (maximum or minimum) coefficient value appears in several consecutive steps, the time of the middle step was used as the time of

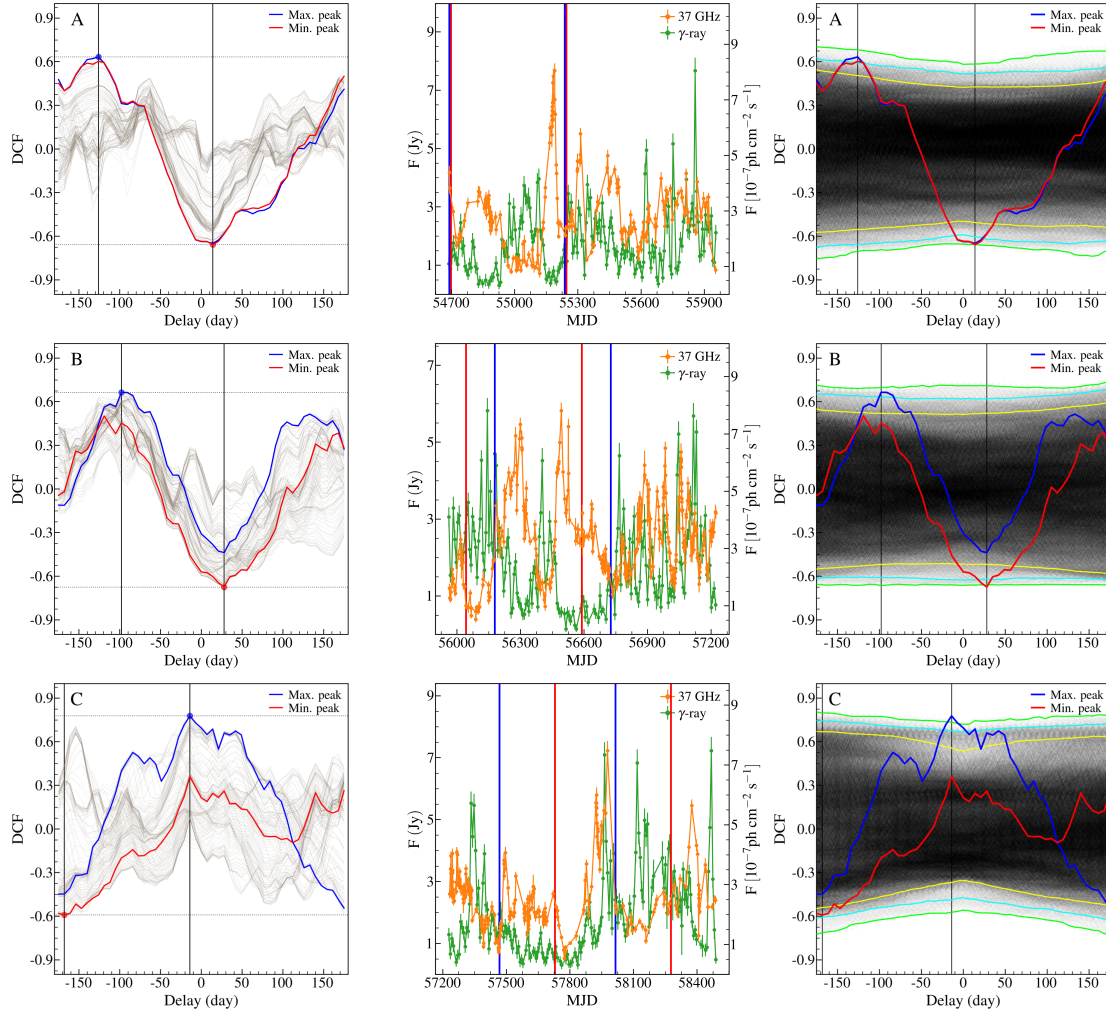


Figure 4. From left to right: DCF curves derived from 1.5-year windows, observed 37 GHz and γ -ray light curves, and the “extremal” DCF curves containing the highest (blue curves) and lowest DCF (red curves) values plotted on top of ~ 15000 DCF curves obtained from random selection. From top to bottom, each row shows the A, B, and C periods, respectively. The 1.5-year time ranges corresponding to the DCF curves with maximum (“Max.”) and minimum (“Min.”) DCF values are marked by blue and red vertical lines, respectively, in the 3.5 year light curves. In the third column, the yellow, cyan, and green curves denote the 95, 99, and 99.9% confidence levels, respectively. The positions of extremal coefficients are denoted by vertical black lines.

the strongest correlation. The panels in the first column of Figure 4 show the results of this search. The 1.5-year time ranges (labeled T1, T2, and T3 for periods A, B, and C, re-

Table 1. The optimum 1.5-year regions found for the γ -ray–37-GHz correlation analysis

Time (MJD)	Delay ¹ (days)	DCF ²
T1: 54697.5 – 55245.0	14	–0.66
T2: 56042.0 – 56589.5	28	–0.67
T3: 57467.0 – 58014.5	–14	0.78

¹ +: radio leading, –: γ -ray leading.

² DCF coefficient values.

spectively) of the selected DCF curves are displayed in the second column of Figure 4.

To construct significance levels, we generated DCF curves for many possible pairs of 1.5-year radio/ γ -ray intervals (in total $\sim 15,000$ DCF curves) for each of the A, B, and C periods by random selection (any duplication was rejected). In the third column of Figure 4, the two “extremal” DCF curves containing the highest and lowest DCF values (shown in the first column of Figure 4) are overlaid onto the $\sim 15,000$ DCF curves produced by the random pair test.

Interestingly, we found that the most negative DCF values exceeded the 99.9% confidence level in periods A and B only, while this was the case only for the most positive DCF value in C. This suggests that the three 1.5-year time ranges (T1, T2, and T3) yielding these extreme DCF values are the origin

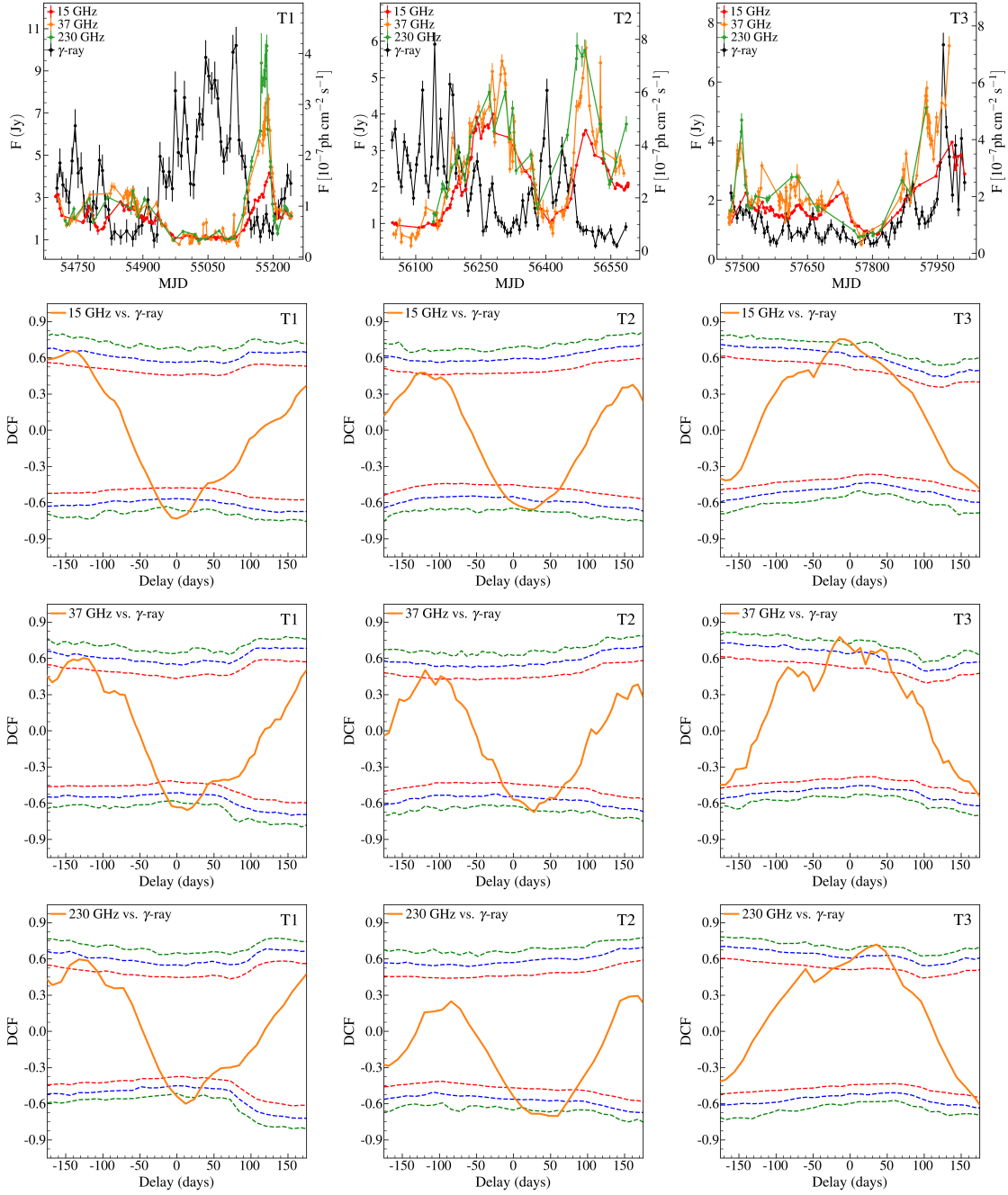


Figure 5. From top to bottom: the radio and γ -ray light curves and the DCF curves from using 15, 37, and 230 GHz radio data, respectively. Columns from left to right correspond to periods $T1$, $T2$, and $T3$, respectively. In each DCF plots, the orange curve indicates the DCF curve. The red, blue, and green solid lines denote the 95, 99, 99.9 % confidence levels, respectively.

of the significant (anti-)correlations between the radio and γ -ray light curves in the A , B , and C periods, respectively. In each of the periods A , B , and C , extreme DCF values tend to appear at similar time delays. This is an actual measurement and not an artifact of external constraints. The light curves vary rapidly; correlated and anti-correlated segments are only a small displacement of the sliding 1.5-year window away

from each other. We summarize the results of our test in Table 1.

3.2.3. DCF curves over the $T1$, $T2$, and $T3$ periods

For the periods $T1$, $T2$, and $T3$, we performed the statistical test in the same manner as in Section 3.2.1, but using all radio bands. Figure 5 shows the results of the DCF analysis between the radio (15, 37, and 230 GHz) and γ -ray light curves. Unsurprisingly, we find significant anti-correlations

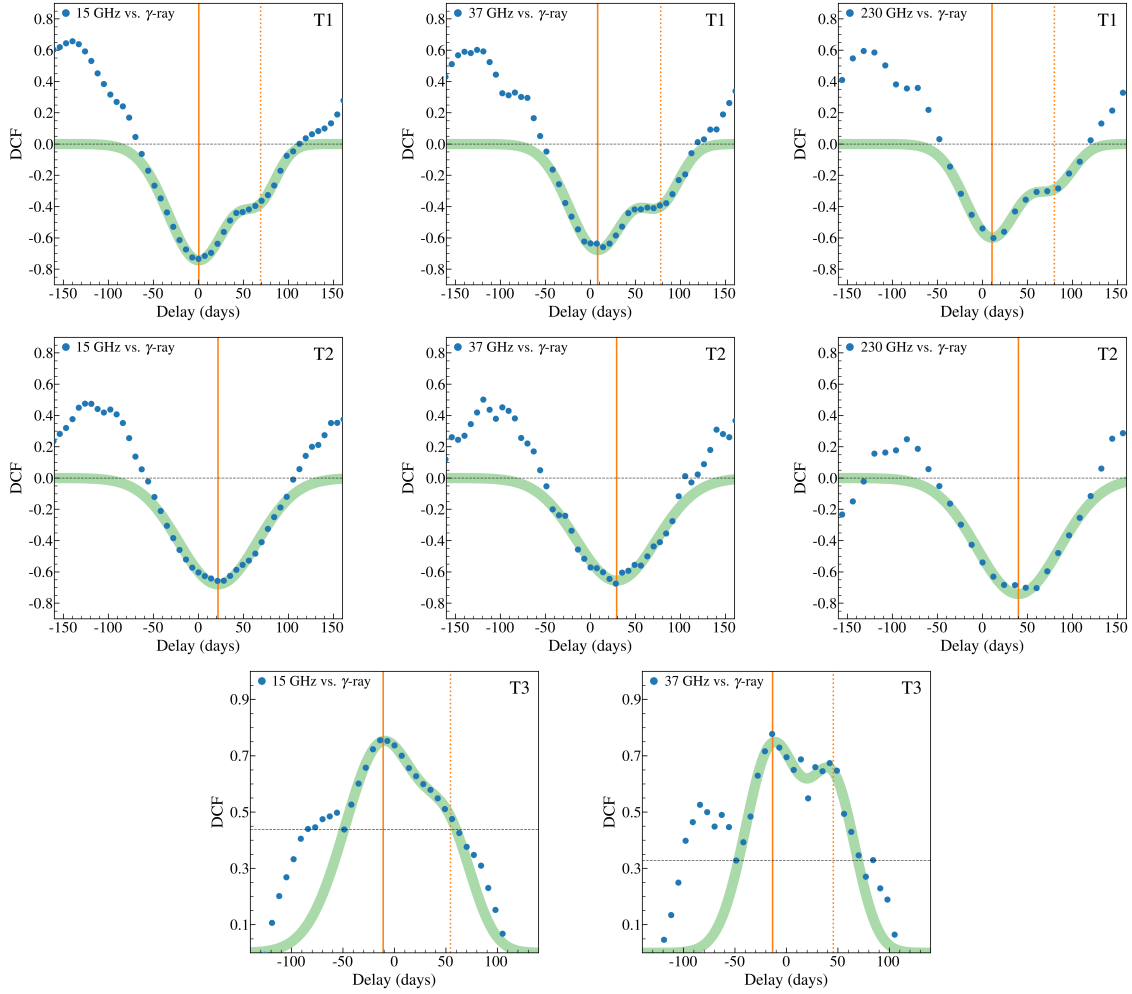


Figure 6. Multi-component Gaussian fits to the DCF curves shown in Figure 5. Thick green curve indicate the best-fit models. DCF peaks are marked with yellow vertical lines: absolute maxima or minima (*solid*) and side-lobe peaks (*dotted*). The fits used only the DCF values exceeding selected thresholds (*horizontal black dashed lines*).

Table 2. Parameters of the best-fit Gaussian models shown in Figure 6

Data	a^1	c^2 (days)	$ w ^3$ (days)
$T1$ at 15 GHz	-0.74 ± 0.01	0.4 ± 0.7	33.6 ± 0.8
$T1$ at 37 GHz	-0.68 ± 0.01	7.9 ± 1.3	31.2 ± 1.4
$T1$ at 230 GHz	-0.60 ± 0.01	10.7 ± 1.2	29.3 ± 1.3
$T2$ at 15 GHz	-0.68 ± 0.01	21.8 ± 1.2	43.3 ± 1.3
$T2$ at 37 GHz	-0.66 ± 0.02	29.0 ± 1.3	44.2 ± 1.6
$T2$ at 230 GHz	-0.74 ± 0.02	39.9 ± 1.4	45.7 ± 1.5
$T3$ at 15 GHz	0.75 ± 0.01	-11.0 ± 1.5	36.7 ± 1.4
$T3$ at 37 GHz	0.73 ± 0.03	-13.5 ± 3.3	26.1 ± 2.9

¹ Peak amplitude of the Gaussian component.

² Peak location of the Gaussian component.

³ Width of the Gaussian component.

in both the $T1$ and $T2$ periods for all radio frequencies. In addition, we find DCF maxima (positive correlations) at delays between about -150 and -100 days, though these are less significant than the anti-correlations. Thus, our DCF results are consistent with the trends in the long-term correlation analysis presented in Section 3.2.1. We also find a significant positive correlation in the $T3$ period.

The location of the negative DCF minima indicates that the radio emission leads the γ -rays. Since the light curves vary rapidly ‘from peak to valley’, a misidentification of corresponding flares can introduce negative correlations at positive time delays. Indeed, the negative delays for the positive correlation peaks in $T1$ and $T2$ indicate that the γ -ray emission leads the radio emission, which is typical for blazars (e.g. Pushkarev et al. 2010). However, the positive correlation between the γ -rays and the 230 GHz data in $T3$ shows the opposite trend. The relatively poor sampling of the 230 GHz data during this period missed the major radio flare that was ob-

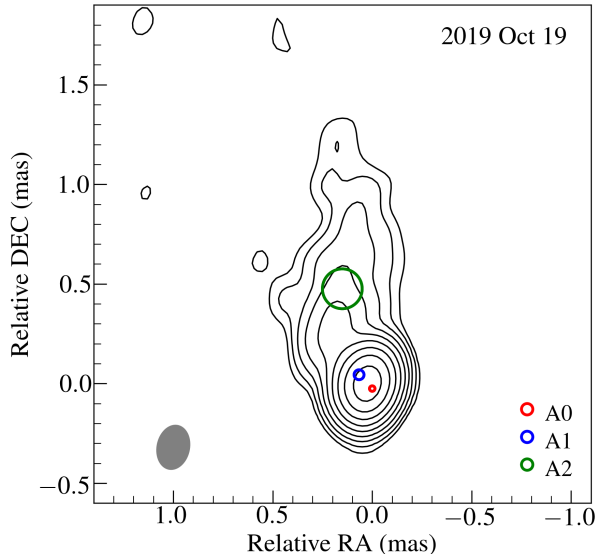


Figure 7. Total intensity image of the 0716+714 jet observed by the VLBA at 43 GHz on 2019 October 19. The contour levels increase by a factor of 2, from 0.25% to 64% of the peak flux (i.e., 0.55 Jy). The synthesized beam size is shown by the ellipse in the *bottom-left* corner. The blue and green circles indicate the mean positions and sizes of A1 and A2 measured in 2008–2019, respectively. The red circle (A0; the core) is located at the map peak and indicates the mean core size (i.e., a FWHM of 0.03 mas).

served in the other two radio frequencies around MJD 57980 completely. In view of this, we were unable to estimate an accurate DCF curve for the 230 GHz data in the T3 period and do not consider it in further analysis.

To identify the precise location and time lag of each DCF peak, we fit one or two Gaussian functions of the form $DCF(t) = a \times \exp[-(t - c)^2 / 2w^2]$, with a , c , and w being the amplitude, delay, and width of the Gaussian profile, respectively, to the data (e.g., Rani et al. 2013; Berton et al. 2018). Figure 6 shows the results. A single Gaussian for T2 and double Gaussian for T1 and T3 were used to better describe the DCF extrema. Table 2 shows the parameters of the best-fit Gaussian models. In all three periods (T1, T2, and T3), the centimeter to millimeter radio light curves are highly correlated/anti-correlated with the γ -ray flux and show extremal coefficient values of very similar magnitude, thus suggesting the same physical processes behind the 15, 37, and 230 GHz fluxes (e.g., Rani et al. 2013; Angelakis et al. 2019). We also noticed that there is a frequency-dependent delay in the DCF peaks. For both the positive and negative correlations, the positions of the maxima and minima are located at larger absolute delay values for higher radio frequencies.

3.3. Jet kinematics

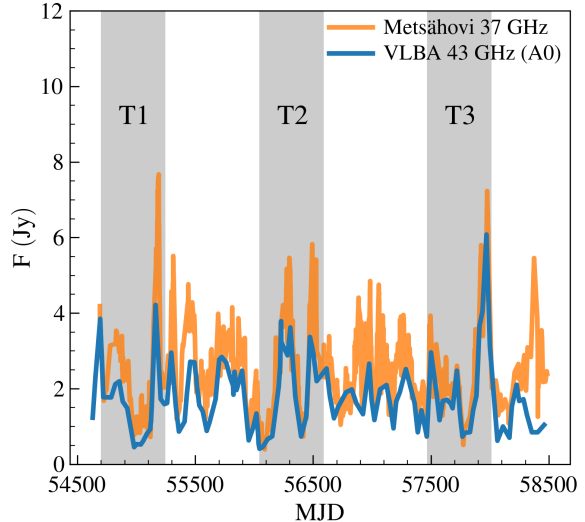


Figure 8. Radio light curves of 0716+714: total flux density at 37 GHz obtained from Metsähovi (orange) and core (A0) flux density at 43 GHz obtained from VLBA (blue).

The activity in the parsec scale jet of 0716+714 has been monitored at 7 mm (43 GHz) by the VLBA-BU-BLAZAR program. To reconstruct the jet structure, we model the Fourier transform of the sky brightness distribution in the (u, v) visibility domain with a number of two-dimensional Gaussian intensity profiles using the *modelfit* task in the Difmap software package (Shepherd 1997). Figure 7 shows the radio jet structure of the blazar on 2019 October 19. We designate the 7 mm core as A0, which is assumed to be the brightest region at the upstream end of the jet flow. Apart from the core, we identify two stationary features, A1 and A2, located at average distances of 0.10 ± 0.02 and 0.53 ± 0.10 mas from the core, respectively, and 14 individual moving knots (B1–B14); here the errors of the mean distances of A1 and A2 from the core are their average sizes. Comparison of the total and the core light curves (see Figure 8) indicates that the core is nearly always the dominant source of the millimeter emission. Table 5 summarizes the parameters of all jet components. Figure 9 shows the knot propagation and the radio and γ -ray light curves.

The B1–B14 jet components show a linear motion except for B7 which was better fit by a quadratic polynomial. We exclude B14 from the further kinematics analysis because it is detected only at three epochs. The ejection epoch T_0 for each of the components B1–B13 was calculated from fits to the RA and DEC coordinate using a linear regression. Due to large errors in T_0 exceeding 0.5 years for the B3, B5, B7, and B10 knots, we calculated the ejection epoch from a linear fit to the radial distance from the core versus time. A complete description of the observations and data calibration will be

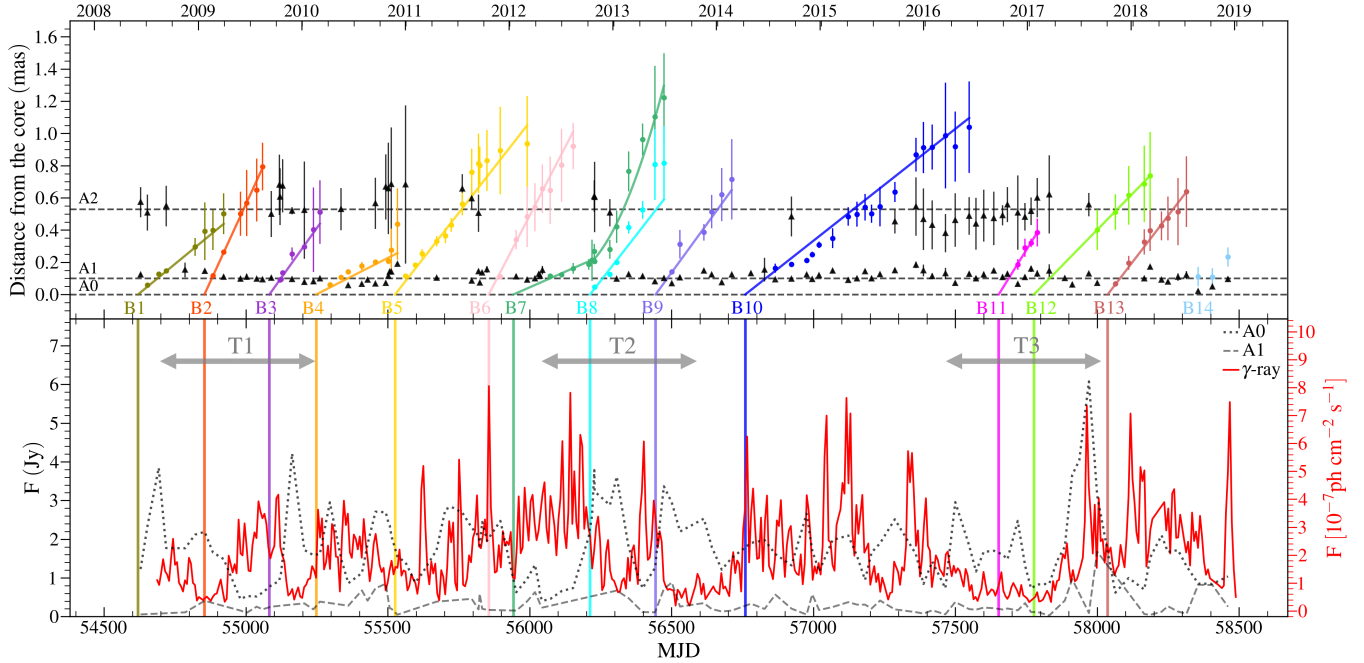


Figure 9. Top: Separation of jet components from the core as function of time. The solid lines represent linear fits to the component positions, dashed lines indicate the positions of the core A0 and the stationary features A1 and A2. Bottom: The 43 GHz light curves of A0 and A1 overlaid on the γ -ray light curve. The component A2 is omitted due to its weak emission. Vertical solid lines mark the epochs of ejection of the newborn jet components.

provided in Weaver et al. (in prep.). The kinematics of the knots is summarized in Table 3.

Table 3. Newborn jet components in 2008–2019

ID	T_0^1 (MJD)	μ^2 (mas/year)	ϕ^3 ($^\circ$)	β_{app}^4 (c)
B1	54620 ± 15	0.53 ± 0.04	21 ± 22	10.0 ± 0.3
B2	54854 ± 2	1.40 ± 0.03	-3 ± 6	26.4 ± 0.2
B3	55083 ± 10	1.04 ± 0.05	-9 ± 4	19.6 ± 0.3
B4	55248 ± 52	0.33 ± 0.04	26 ± 5	6.2 ± 0.2
B5	55526 ± 32	0.82 ± 0.03	23 ± 2	15.6 ± 0.2
B6	55856 ± 8	1.24 ± 0.05	23.3 ± 1.2	23.4 ± 0.3
B7	55943 ± 79	1.07 ± 0.11	30 ± 8	20.1 ± 0.6
B8	56213 ± 2	0.83 ± 0.13	34 ± 6	15.6 ± 0.7
B9	56444 ± 6	0.88 ± 0.07	5 ± 5	16.7 ± 0.4
B10	56760 ± 61	0.51 ± 0.03	25 ± 2	9.6 ± 0.2
B11	57653 ± 1	1.04 ± 0.12	8 ± 12	19.6 ± 0.7
B12	57777 ± 4	0.66 ± 0.03	5 ± 8	12.4 ± 0.2
B13	58037 ± 2	0.84 ± 0.03	27 ± 4	15.8 ± 0.2

¹ Ejection time.

² Proper motion.

³ Direction of motion (North through East).

⁴ Apparent velocity in units of speed of light.

The apparent velocities (β_{app}) of the knots B1–B13 are located in the range from 6 to 26 c . The direction of the motion varies between -9° (Western) and 34° (Eastern) as measured from North. On average, the knots were ejected from the core every 0.8 years. This is a bit higher than what Jorstad et al. (2017) expected. However, if we exclude the long quiescent period between B10 and B11 (i.e., 893 days), the ejection interval becomes 0.6 years. Two knots were found in each of the T1, T2, and T3 periods: B2–B3 in T1, B8–B9 in T2, and B11–B12 in T3. The timing between ejections and radio/ γ -ray flares differs from knot to knot. However, a consistent behavior can be seen in T2: each ejection coincides with the decaying phase of a γ -ray flare and the rising phase of a radio flare. In the case of T3, the ejection of B11 seems not to be correlated with any significant events at both radio and γ -rays. However, strong radio and γ -ray flares started rising just after the ejection of B12 almost simultaneously.

We further investigated the global kinematic properties of the 0716+714 jet. Figure 10 shows the results of the analysis of component motions, component sizes (FWHM), and position angles. The parameters in the radial distance domain (r) show complex behavior with large scatter, except for the motion in declination (see the top panel of Figure 10). We used linear regressions to approximate the global behaviors of the parameters of the knots. As was shown above, there is a stationary feature A2 at about ~ 0.53 mas from the core. This feature could be a transition region or a shock which

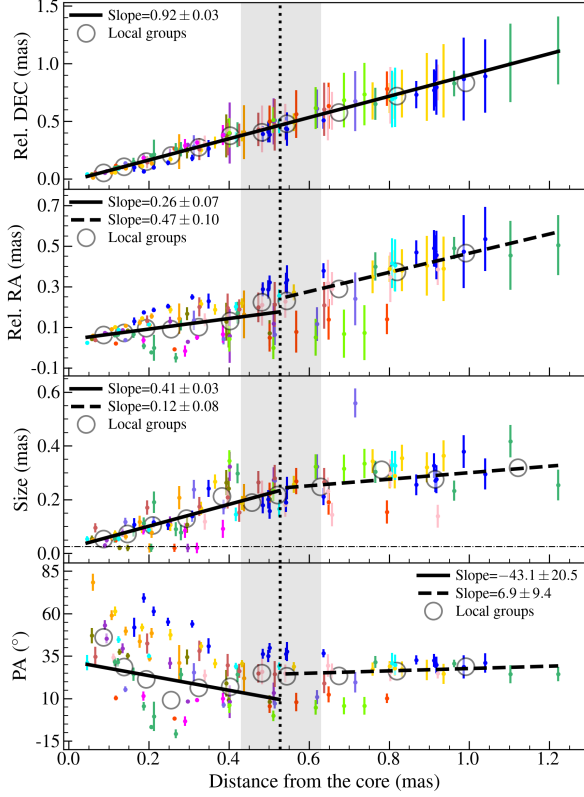


Figure 10. From top to bottom: relative DEC and RA, size, and position angle (PA; North through East, where 0° corresponds to North) as function of the distance from the core for the knots $B1$ – $B13$ obtained from the model fits to the VLBA images. Data colors are the same as in Figure 9. The black solid/dashed lines indicate linear regressions. For RA, size, and PA, regressions are performed separately for distances within and beyond the mean position of $A2$ (i.e., 0.53 mas) which is denoted by the vertical black dotted line. The shaded gray color region represents the mean FWHM of $A2$ (i.e., 0.2 mas) which shows the overall size of the region. The empty gray circles show the mean variations of the parameters by averaging 10 consecutive points each. Lower limits on sizes (third panel from top) are indicated by the horizontal dot-dashed line.

leads to a change in the jet physical conditions (e.g., Kadler et al. 2008; Larionov et al. 2013; Beuchert et al. 2018). Thus, we performed the analysis for two groups of data separately: one with $r < 0.53$ mas and the other with $r \geq 0.53$ mas. The angular resolution of our data is insufficient to apply the analysis on smaller scales (e.g., less than 0.2 mas). Thus, the stationary feature $A1$ was excluded from this analysis.

The jet components move in norther direction. We quantify their collective motion by assuming the relationship $d_{xy} \propto kr$, where d_{xy} is either the relative RA (x) or DEC (y) of the knots, r is the radial distance from the core, and k is the slope. The linear slope of the motion in the y direction is $k \sim 0.9$, i.e. an almost one-to-one match with the radial distance. However, the slope of the motion along the x -axis, which is ap-

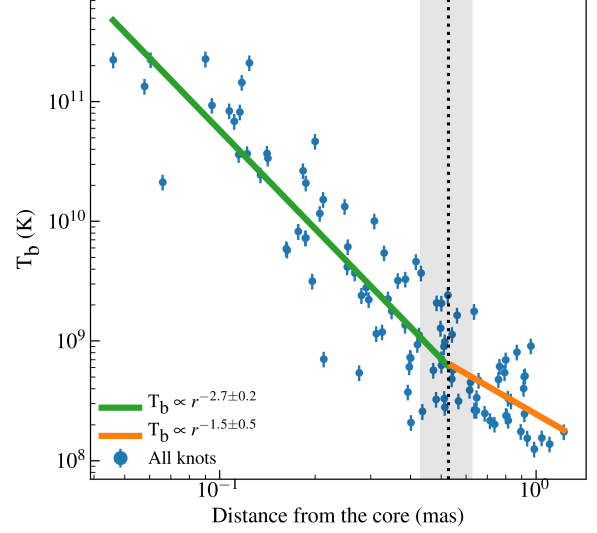


Figure 11. Observed brightness temperatures of all knots ($B1$ – $B13$) as a function of the distance from the core. The analysis is the same as in Figure 10, but using a power-law ($T_b \propto r^\epsilon$). The uncertainties of the brightness temperatures were assumed to be 15% (Beuchert et al. 2018).

proximately perpendicular to the jet axis, is much smaller, meaning that the motion is primarily in the y direction. Interestingly, at least one knot shows a curved trajectory, which indicates a bend in the jet (see also Larionov et al. 2013; Rani et al. 2015). Indeed, from calculating d_x we found that there are two separate linear trends in the transverse motion: one with $k \sim 0.26$ for $r < 0.53$ mas, and one with $k \sim 0.47$ for $r \geq 0.53$ mas. This indicates that there is a change in the jet direction at $A2$.

The position angles show large variations out to $A2$, indicating a bending of the jet. Due to the large scatter, the position angle data are not well described by a linear trend. However, the outer region (i.e., downstream from $A2$) shows a clear linear trend. It should be noted that the uncertainties of the slopes are quite large. This implies that the angle variations are complicated and linear trend lines cannot fully describe the behavior of the position angle as function of core distance. We form groups by averaging over 10 consecutive points (total 110 model jet components) in the r domain; as for the component size, seven lower limits on the size were rejected from the analysis, and the last bin contains three data points. The grouped position angles indicate that the jet axis moves from East to North (from about 50° to 10°) up to a radial distance of ~ 0.3 mas, after which the jet bends back toward the eastern direction. However, the variation in the position angle is relatively weak beyond ~ 0.3 mas from the core before converging at about 30° .

Figure 11 shows the distribution of the observed brightness temperatures versus radial distance (Kovalev et al. 2005;

Jorstad et al. 2017). Seven outliers, which correspond to the unresolved jet components shown in Figure 10, were excluded from the analysis. We fit power-law models (i.e., $T_b \propto r^\epsilon$) to the brightness temperature data. To investigate any transition at the position of A2, we again divided the distribution in the same manner as in Figure 10. The resultant power-law indices are $\epsilon = -2.7 \pm 0.2$ and $\epsilon = -1.5 \pm 0.5$ in the inner and outer regions, respectively. The power-law index within the inner region is consistent with the values obtained from the parsec-scale jets of other blazars (e.g., Kadler et al. 2008; Rani et al. 2015; Kravchenko et al. 2016). The notable change in the brightness temperature gradient at the location of A2 is an indication of a sudden change in the physical properties of the jet (e.g., Böttcher et al. 2005; Fromm et al. 2013; Beuchert et al. 2018).

Rani et al. (2014) suggested a connection between the γ -ray emission and the inner jet position angle (near the core). We investigated the variations in the mean position angle of the knots as shown in Figure 12. For each knot ($B1$ – $B13$), the mean position angle and its location in the time domain were determined by calculating the average values of the position angles and observing epochs (see the model-fit results in Table 5). Interestingly, the three periods with significant radio-to- γ -ray correlations (i.e., $T1$, $T2$, and $T3$) correspond to epochs of smaller mean position angles (below 20°). This indicates that the global jet direction was more aligned toward North during those periods. Changes in the jet orientation can be due to propagation of jet components at different position angles (Gómez et al. 2011; Casadio et al. 2015a; Pushkarev et al. 2017). This might determine the association of the knot with a γ -ray flare by changing the Doppler factor and viewing angle of the jet (e.g., Casadio et al. 2015b). Thus, we suggest that the northernmost position angles corresponds to closer alignment of the jet with the line of sight, with the corresponding beaming effects in turn leading to the correlated radio and γ -ray flares (see also Jorstad et al. 2001; Rani et al. 2014; Liodakis et al. 2018a, for discussions of different beaming effects between the radio and γ -ray emitting regions).

4. DISCUSSION

4.1. Interpretation of radio- γ -ray correlations and time lags

The occasional occurrence of a significant correlation and/or anti-correlation between the radio and *Fermi*-LAT γ -ray activity might indicate that the variability in these bands is initiated by the same physical process. However, causality arguments in combination with the typical \lesssim day scale γ -ray variability time scales constrain the γ -ray emitting region to a size of $\lesssim 10^{16}$ cm. Such a compact emission region is generally found to be optically thick to synchrotron self-absorption (SSA) at radio wavelengths. Therefore, the

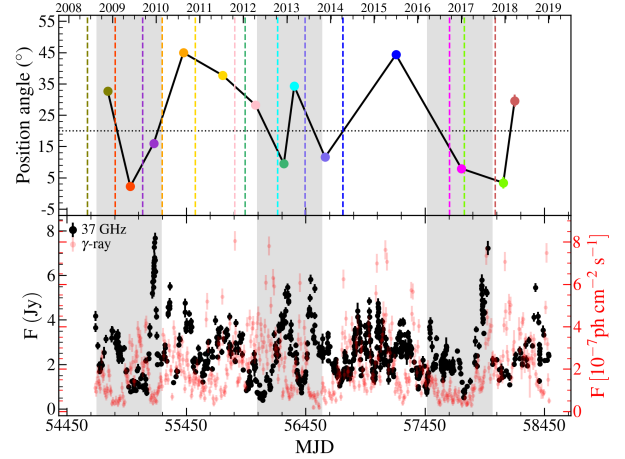


Figure 12. *Top:* mean position angles of the jet knots at their mean epochs. Colors are the same as in Figure 9. The vertical dashed lines indicate the ejection times of the knots. The horizontal dotted line marks 20° . The gray shaded regions indicate the periods $T1$, $T2$, and $T3$, respectively. *Bottom:* the observed radio and γ -ray light curves.

γ -ray emission is likely to be produced up-stream from the 37 GHz radio core. This is in agreement with previous observations of γ -ray bright blazars which suggest that a time lag between γ -ray and radio emission is due to the opacity effect (Pushkarev et al. 2010; Rani et al. 2013; Ramakrishnan et al. 2016; Liodakis et al. 2018b). In general, the γ -rays precede the radio emission, thus suggesting an upstream production of the γ -rays with respect to the radio emitting site (Fuhrmann et al. 2014; Max-Moerbeck et al. 2014b).

Using VLBA observations, we found that all γ -ray flares which were correlated with radio flares, were accompanied by the ejection of a VLBI jet component: $B2$ and $B3$ in $T1$, $B8$ and $B9$ in $T2$, and $B12$ (or $B13$) in $T3$. The calculated ejection epochs (T_0) are expected to coincide with the time when the knot passes through the radio core. Thus, this could explain the estimated T_0 locations of the knots relative to the evolutionary stages of the 43 GHz core flares.

We find that the ejection times of $B3$, $B8$, and $B9$ are located at the rising stage of a radio flare, whereas that of $B2$ is near the peak of a radio flare. However, the actual peaks of the radio flares can be a product of superposed underlying components (e.g., León-Tavares et al. 2011), and thus care should be taken in the comparison. The position of T_0 in the radio light curves might be affected by variable beaming effects (e.g., Liodakis et al. 2018a) and/or complex trajectories of the knots. Larionov et al. (2013) suggested that a shock wave moving down a helical path along the jet can explain the observed flaring features in S5 0716+714. This might play a crucial role for the individual knots, thus resulting in less accurate estimates of T_0 or distortion of the observed flaring features (see also Kravchenko et al. 2020,

for the significantly bent structure even at μas scales). Furthermore, there could be a substantial change in the velocity of the knots due to the interaction with the standing shocks (e.g., [Schinzel et al. 2012](#); [Liodakis 2018](#)) or a bent-jet structure (e.g., [Rani et al. 2015](#)). This suggests a transition from smaller velocities in a region near the radio core to higher velocities beyond this region. The knot *B2* has the highest apparent velocity ($26c$) in our observations, and this might affect the estimation of its T_0 making it appear further downstream from its true ejection epoch. Given the overall trend in T_0 of the knots (i.e., a position between the γ -ray and radio flares), however, we suggest that these knots likely caused the notable radio flares in *T1* and *T2* by interacting with the radio core.

We therefore propose the following scenario to explain the marginal positive radio– γ -ray correlations with leading γ -ray emission as well as the more significant anti-correlation with radio leading features: A new jet component is being ejected from the central engine, accompanied by efficient relativistic particle acceleration, possibly mediated by internal shocks (e.g., [Spada et al. 2001](#); [Sokolov et al. 2004](#); [Sokolov & Marscher 2005](#); [Graff et al. 2008](#); [Böttcher & Dermer 2010](#); [Chen et al. 2011](#); [Joshi & Böttcher 2011](#); [Zhang et al. 2015](#); [Baring et al. 2017](#); [Böttcher & Baring 2019](#)). Both high-frequency (mm–IR–optical) synchrotron radiation as well as external (e.g., IR from the dust torus) radiation fields are intense in that region and serve as efficient targets for Compton scattering to produce a bright γ -ray flare, while the emission region is still opaque to SSA. Subsequent radio flares are produced by the passage of the disturbance through the radio cores at the various frequencies, with radio flares occurring earlier at the higher radio frequencies.

Visual inspection of the radio and γ -ray light curves suggests that the significant radio– γ -ray anti-correlations in *T1* and *T2* are due to long-lasting dips in the γ -ray light curves following radio flares by a few – few tens of days. We here suggest that this may be either due to efficient radiative cooling of γ -ray emitting electrons or due to the emission region leaving the influence of dense target radiation fields for Compton scattering.

The best-fit time delays may be used to estimate the corresponding propagation distances ($d_{\gamma\text{r}}$) in terms of β_{app} (Table 3) for each period and frequency. We considered the mean β_{app} values of the knots ejected in the *T1* and *T2* periods separately: *B2–B3* for *T1* and *B8–B9* for *T2*. In the case of *T3* (*B11–B12*), *B13* was used instead of *B11* due to its closer timing to the flares. Using the relation $\Gamma \approx (1 + \beta_{\text{app}}^2)^{1/2}$ (e.g., [Pushkarev et al. 2012](#); [Karamanavis et al. 2016](#)), we obtained the following set of parameters: $\beta_{\text{app}} = 23$ and $\theta_{\text{obs}} = 2.5^\circ$ for *T1*, $\beta_{\text{app}} = 16$ and $\theta_{\text{obs}} = 3.6^\circ$ for *T2*, and $\beta_{\text{app}} = 14$ and $\theta_{\text{obs}} = 4.1^\circ$ for *T3*. With these estimates, we calculated the $d_{\gamma\text{r}}$ values (see Table 4) using the relation

Table 4. The $d_{\gamma\text{r}}$ values obtained from the delays of the significant correlations in *T1*, *T2*, and *T3*.

	<i>T1</i> ¹	<i>T2</i> ¹	<i>T3</i> ²
$d_{\gamma,15\text{GHz}}$ (pc)	0.1 ± 0.2	3.6 ± 0.2	1.4 ± 0.2
$d_{\gamma,37\text{GHz}}$ (pc)	2.7 ± 0.4	4.7 ± 0.2	1.7 ± 0.4
$d_{\gamma,230\text{GHz}}$ (pc)	3.6 ± 0.4	$< 6.5^3$	-

¹ Negative correlation with the radio leading feature.

² Positive correlation with the γ -ray leading feature.

³ considered to be overestimated due to the sparse sampling.

(e.g., [Ramakrishnan et al. 2014](#)): $d_{\gamma\text{r}} = \frac{\beta_{\text{app}} c \Delta t_{\gamma\text{r}}}{\sin \theta (1+z)}$. The resulting propagation distances are listed in Table 4.

For the flaring episode in *T3*, we can estimate the location of the γ -ray production site by assuming the location of the 15 GHz radio core from the central engine to be 7–8 pc as reported by [Pushkarev et al. \(2012\)](#) and [Butuzova \(2018\)](#). With the $d_{\gamma,15\text{GHz}}$ value of 1.5 pc, the γ -ray site can be estimated to be located 5.5–6.5 pc from the central engine. [Rani et al. \(2015\)](#) reported the location of the 43 GHz core to be at ~ 6.5 pc. This might be explaining the occurrence of the radio and γ -ray flares in close proximity to each other in *T3*.

For *T1* and *T2*, the delays of the positive correlations, with the γ -rays leading, decrease with higher frequencies, as expected. The delays in *T1* and *T2* at 15 GHz are roughly -140 and -120 days, respectively. From these delays, $d_{\gamma\text{r}}$ can be estimated as 47 and 20 pc for *T1* and *T2*, respectively. Given the locations of the 15 and 43 GHz cores suggested by previous studies (i.e., 6–8 pc), such large values seem to be highly overestimated. We suggest that this could be attributed to a complicated path (e.g., helices) of the moving disturbances and/or significant changes in β_{app} of the knots. Assuming the viewing angles found in Section 4.1, we found that the $d_{\gamma\text{r}}$ values are comparable to the expected locations of the radio cores with the β_{app} values around 3.5 for *T1* and 6.0 for *T2*. Thus, we suggest that strong moving disturbances produce the γ -ray flares in *T1* and *T2* at subparsec scales from the jet apex and undergo significant velocity changes (possibly with variable viewing angles) in their motions by the time they reach the radio cores (see also [Geng et al. 2020](#), for a subparsec-scale origin of γ -rays in S5 0716+714).

Further physical insight will be gained by comparing the observed time delays to the radiative cooling time scales of electrons emitting synchrotron at GHz frequencies ($\gamma \sim 100$) and Compton emission at GeV γ -ray energies ($\gamma \sim 10^4 - 10^5$). These can be estimated as $t_{\text{rad}}^{\text{obs}} \approx 1.2 \times 10^5 B_{-1}^{-2} \delta_1^{-1} (1 + C)^{-1} \gamma^{-1}$ days, where $B = 0.1 B_{-1}$ G is the magnetic field, $\delta = 10 \delta_1$ the Doppler factor, and $C \equiv \nu F_V^C / \nu F_V^{\text{sy}} \sim 1$ is the Compton dominance parameter. This corresponds to observed cooling time scales of $\sim 60 B_{-1}^{-2} \delta_1^{-1}$ days for radio-emitting electrons and $\lesssim 15 B_{-1}^{-2} \delta_1^{-1}$ hours for γ -ray emit-

ting electrons. The latter time scale is well consistent with the \sim day scale γ -ray variability and suggests that there must be on-going particle acceleration during the flaring periods that last several days. 37-GHz-radio-emitting electrons (with Lorentz factor $\gamma'_{37} \approx 94 B_{-1}^{-1/2} \delta_1^{-1/2}$) that may have been co-accelerated with the γ -ray emitting electrons in the γ -ray emission region, will not have had time to cool significantly by the time they reach the radio emitting zone. Hence, if a γ -ray flaring event produces excess electrons both low ($\gamma \sim 100$) and high ($\gamma \gtrsim 10^4$) energies simultaneously, these excess radio emitting electrons will not have been affected by radiative cooling by the time the emission region reaches the radio core (becoming optically thin to SSA), thus leading to positively correlated variability among the radio and γ -ray bands with leading γ -ray activity and delay times decreasing with increasing frequencies.

The significant anti-correlations between radio and γ -ray activity, with radio flares preceding dips in the γ -ray light curve by several – several tens of days and time delays increasing with increasing frequencies, may be a consequence of efficient radiative cooling of γ -ray emitting electrons. The delay between the radio flares and the γ -ray dips could possibly originate from synchrotron self-Compton (SSC) cooling on the light crossing time scale through the radio core: as the radio flare evolves, the synchrotron photon field in the radio core builds up, leading to SSC emission (and cooling) of the high-energy electrons. Thus, if the observed time delay represents the light-crossing time scale through the emission region, it would indicate a size of the radio core of $R_{\text{radio}} \sim 2 \times 10^{17} \delta_1 \Delta t_1$ cm, where $\Delta t = 10 \Delta t_1$ days is the time delay. The resulting SSC emission is expected to emerge in X-rays, so this scenario would predict that the radio flare(s) should be correlated with X-ray flares. There have been a number of previous studies (e.g., Vittorini et al. 2009; Liao et al. 2014; Rani et al. 2015; MAGIC Collaboration et al. 2018) that report correlated radio/X-ray emission in S5 0716+714. Given sparse sampling of the X-rays (e.g., Rani et al. 2013; Wierzcholska & Siejkowski 2015) and the concave X-ray spectrum generated by both synchrotron and IC (e.g., Liao et al. 2014; MAGIC Collaboration et al. 2018), however, more detailed hard X-ray observations would be necessary for clarity. It is worth noting that the 230 GHz data suffers relatively sparse sampling in $T2$. This prevents us from measuring the delay of the anti-correlation accurately in this period. Thus, we consider that the $d_{\gamma,230\text{GHz}}$ of $T2$ is significantly overestimated and might actually be smaller (e.g., around 5.0–5.5 pc) given the opacity effect in the jet.

Alternatively, the motion of the emission region out of the core region of the AGN might result in the energy densities of target radiation fields for Compton scattering dropping off rapidly. With the location of the 37 GHz radio core assumed to be ~ 7 – 8 pc from the black hole, the radio– γ -ray delay then

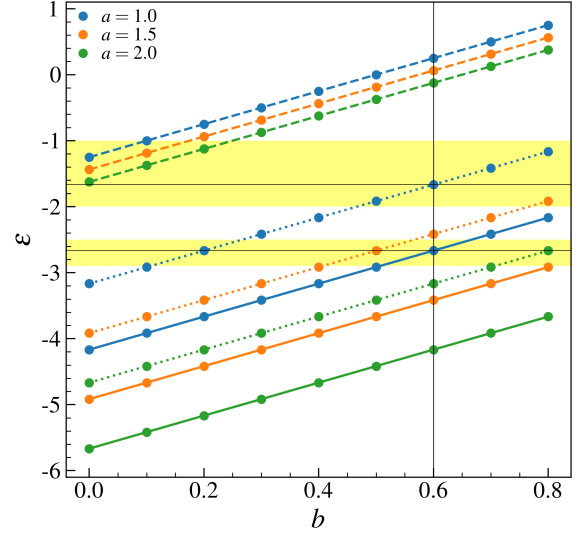


Figure 13. Calculated ϵ as a function of b . a depends on the dominant magnetic field component: from 1 (toroidal) to 2 (poloidal). The dashed, dotted, and solid lines indicate ϵ_c , ϵ_a , and ϵ_s respectively. The yellow regions denote the power-law dependencies of the inner and outer regions with their uncertainties. The most probable estimates ($\epsilon_s = -2.7$ and $\epsilon_a = -1.7$) are marked by the vertical and horizontal lines.

implies a distance of ~ 10 pc from the central engine, where the dips in the γ -ray light curve are produced. This is a characteristic size of dusty, infrared-emitting tori of AGN, which have often been invoked as the source of the dominant target photon field for Compton scattering in low- and intermediate-frequency peaked BL Lac objects (e.g., Abdo et al. 2011b; Ackermann et al. 2012; Böttcher et al. 2013). It is therefore quite plausible that the reason for the delayed γ -ray dips is the γ -ray emission region leaving the sphere of influence of the dust-torus radiation field.

4.2. Evolution of the parsec scale jet

Considering the three primary evolutionary stages in the energy losses of the travelling shocks: Compton, synchrotron, and adiabatic (Marscher et al. 1992), Rani et al. (2015) derived the three power-law dependencies of the brightness temperature on the radial distance from the core (Lobanov & Zensus 1999) in the 0716+714 jet: $\epsilon_c = [11 - s - a(s+1)]/8 + [b(s+3)]/2 - 2$ for Compton loss, $\epsilon_s = -[4(s-1) + 3a(s+1)]/6 + [b(s+3)]/2 - 2$ for synchrotron loss, and $\epsilon_a = [2(5-2s) - 3a(s+1)]/6 + [b(s+3)]/2 - 2$ for adiabatic loss, where a , b , and s are the power-law scaling indices of the magnetic field $B \propto r^{-a}$, Doppler factor $\delta \propto r^b$, and electron distribution $N(\gamma) \propto \gamma^{-s}$, respectively (see also Schinzel et al. 2012, for the case of the quasar 3C 345). We employed this approach to interpret our results on the observed brightness temperature. a can be set to be 1 or 2 for toroidal and poloidal magnetic fields, accordingly. How-

ever, we also considered an intermediate value of 1.5 for s (Lobanov & Zensus 1999). Given the possible variations in Doppler factor (e.g., Schinzel et al. 2012; Rani et al. 2015), we used b with values between 0 and 1. Figure 13 shows the calculated ϵ with the typical value of $s = 2$ (optically thin spectral index $\alpha \sim -0.5$ from $S_\nu \propto \nu^\alpha$). We find that the combination of $a = 1$ and $b = 0.6$ nicely corresponds to our observed power-law dependencies: $\epsilon_s = -2.7$ and $\epsilon_a = -1.7$ for the inner and outer regions, respectively. This implies that the propagating shocks suffer strong radiative cooling via synchrotron losses at first, then adiabatic losses become prominent as the shocks pass the standing shock A2.

Such changes in the brightness temperature gradient could be caused by a recollimation shock (RCS) and compression of the plasma flow, thus suggesting the stationary feature A2 being a RCS (Kadler et al. 2008). One can expect an increase in the expansion rate of the propagating blobs beyond the RCS, which is supposed to be an overpressured region with respect to the nearby environment (e.g., Beuchert et al. 2018). This is consistent with our estimation above: $\epsilon \sim \epsilon_a$, after the A2 region. The variations in the component size shown in Figure 10, however, indicate that the expansion became less pronounced after A2. This might be indicating that A2 is a standing feature induced by a bend, rather than recollimation (e.g., Jorstad et al. 2001; Rani et al. 2015). The notable changes in the transverse motion and position angle beyond A2 in Figure 10, support such a standing oblique shock scenario (see Jorstad et al. 2001; Ramakrishnan et al. 2014). Larionov et al. (2013) also concluded the stationary feature (their knot K2) belongs to a bending point accompanied by kinematic changes of a moving knot around the standing component. We suggest that collision with the ambient medium or magneto-hydrodynamical instabilities resulted in the formation of the structure.

5. SUMMARY

We have analyzed the long-term cm- and mm-radio and γ -ray light curves of the blazar 0716+714 to explore the connection between high- and low-energy radiation and to pinpoint the production site of the high-energy emission. By using VLBA observations, we were able to probe the parsec-scale jet activity in detail. Our primary conclusions are the following:

1. We found three significant correlation signals between the radio (15, 37, and 230 GHz) and γ -ray light curves in 2008–2019. To identify the epochs from which these signals originate, we split the light curves into segments and found three 1.5-yr-periods of interest: two ($T1$ and $T2$) with an anti-correlation and one ($T3$) with a positive correlation. All these correlations exceed significance levels of 99.9% and peak at the time delays within 40 days (i.e. radio leads γ -ray emission)

in case of an negative correlation and -14 days (γ -ray leads radio emission) in case of a positive correlation.

2. Using VLBA maps, we found three stationary jet features including the core, which dominates in the radio emission. The kinematic analysis revealed 14 jet components (including B14 which is excluded from the analysis) moving downstream the jet. Their apparent velocities range from 6 to $26c$, and the average ejection rate is estimated of ~ 0.8 years. Each of the three significant radio/ γ -ray correlation signals was accompanied by two (for $T1$ and $T2$) or one (for $T3$) moving jet components. We found that these components emerged from the core when radio flares were growing (i.e., onset/rising/peaking).
3. The observed radio/ γ -ray correlations can be attributed to jet components that are being newly ejected from the central engine. During their downstream propagation along the jet, efficient relativistic particle acceleration occurs, possibly mediated by internal shocks. Internal/external radiation fields are sufficient to produce a γ -ray flare. Subsequent flares at radio frequencies are expected to occur as the moving disturbance passes through the radio cores.
4. In each of the $T1$ and $T2$ periods, a marginal positive (γ -ray leading) radio/ γ -ray correlation as well as a more significant anti-correlation (radio leading) were found. We suggest that these two correlation signals are connected: a γ -ray flare at subpc-scales and a subsequent radio flare/ γ -ray dip at pc-scales, produced by a strong moving jet component. The γ -ray dip can be explained by efficient radiative cooling of γ -ray emitting electrons ($\gamma \sim 10^4$ – 10^5), possibly due to shock-compressed, stronger magnetic field in the emission region, or the emission region leaving the influence of dense radiation fields required for IC.
5. For the significant radio/ γ -ray correlation found in $T3$, our estimates ($d_{\gamma r}$) point toward a γ -ray production site located 5.5–6.5 pc from the jet apex. Positively correlated variability between radio and γ -ray bands indicates that the radio emitting electrons have not enough time to cool down significantly by the time they reach the radio core where the jet becomes transparent at radio frequencies.
6. The overall motions of the jet components are complicated and show highly variable position angles, particularly within ~ 0.4 mas from the core. The observed brightness temperature decreases along the jet following a power-law. The power-law index is initially -2.7 ± 0.2 and changes to -1.5 ± 0.5 at the position

of the stationary feature A2 (~ 0.53 mas from the core). This indicates a change in the energy losses from being synchrotron-dominated to adiabatically-dominated.

ACKNOWLEDGMENTS

DK acknowledges the support from the National Research Foundation of Korea (NRF) through the next generation fellowship 2019R1A6A3A13095962. ST and DK acknowledge the support from the NRF grant 2019R1F1A1059721. The work of EVK is supported in the framework of the state project “Science” by the Ministry of Science and Higher Education of the Russian Federation under the contract 075-15-2020-778. The work of MB is supported by the South African Research Chairs Initiative (SARChI) of the Department of Science and Innovation and the National Research Foundation⁶ of South Africa through SARChI grant UID 64789. JLG acknowledges the support of the Spanish Ministerio de Economía y Competitividad (grants AYA2016-80889-P, PID2019-108995GB-C21), the Consejería de Economía, Conocimiento, Empresas y Universidad of the Junta de Andalucía (grant P18-FR-1769), the Consejo Superior de Investigaciones Científicas (grant 2019AEP112), and the State Agency for Research of the Spanish MCIU through the Center of Excellence Severo Ochoa award for the Instituto de Astrofísica de Andalucía (SEV-2017-0709). VR acknowledges the support from the FONDECYT post-doctoral grant 3190878. The Submillimeter Array is a joint project between the Smithsonian Astrophysical Observatory and the Academia Sinica Institute of Astronomy and Astrophysics and is funded by the Smithsonian Institution and the Academia Sinica. This publication makes use of facilities and data obtained at the Metsähovi Radio Observatory, operated by Aalto University, Finland This research has made use of data from the OVRO 40-m monitoring program (Richards et al. 2011), supported by private funding from the California Institute of Technology and the Max Planck Institute for Radio Astronomy, and by NASA grants NNX08AW31G, NNX11A043G, and NNX14AQ89G and NSF grants AST-0808050 and AST- 1109911. This study makes use of 43 GHz VLBA data from the VLBA-BU Blazar Monitoring Program (VLBA-BU-BLAZAR; <http://www.bu.edu/blazars/VLBAproject.html>), funded by NASA through the Fermi Guest Investigator Program. The VLBA is an instrument of the National Radio Astronomy Observatory. The National Radio Astronomy Observatory is a facility of the National Science Foundation operated by Associated Universities, Inc. This work makes use of public Fermi data obtained from *Fermi* Science Support Center (FSSC). *facilities*: OVRO, Metsähovi, SMA, VLBA, *Fermi*-LAT *software*: AIPS, Difmap, *Fermi* Science Tools, Python

7. We found that during the periods of significant radio/ γ -ray correlations (i.e., $T1/T2/T3$) the average position angle of the jet components was smaller than about 20° . This is consistent with a closer alignment of the jet with the line of sight when the jets points toward the north, leading to an enhancement of beaming effects.

APPENDIX

A. VLBI JET COMPONENTS

Table 5. Gaussian model-fit parameters of the BU-43 GHz knots

Date	MJD	Comp.	Flux (Jy)	Distance ^a (mas)	Position angle ^a ($^{\circ}$)	Rel. RA (mas)	Rel. DEC (mas)	FWHM (mas)	T _b (K)	UL _{T_b} ^b
2008.45	54629	A0	1.23±0.06			0.000±0.005	0.00±0.01	0.039±0.007	6.1 × 10 ¹¹	F
		A1	0.06±0.01	0.12±0.01	38.1±2.0	0.076±0.006	0.10±0.01	0.020±0.011	1.0 × 10 ¹¹	T
		A2	0.05±0.01	0.57±0.09	11.5±2.5	0.115±0.048	0.56±0.10	0.181±0.035	1.2 × 10 ⁹	F
2008.51	54653	A0	2.33±0.12			0.000±0.005	0.00±0.01	0.020±0.004	4.4 × 10 ¹²	T
		B1	0.54±0.03	0.06±0.01	47.0±4.6	0.042±0.006	0.04±0.01	0.055±0.011	1.3 × 10 ¹¹	F
		A2	0.07±0.01	0.51±0.11	17.1±3.7	0.150±0.058	0.49±0.12	0.249±0.038	8.3 × 10 ⁸	F
2008.62	54693	A0	3.85±0.19			0.000±0.005	0.00±0.01	0.047±0.006	1.3 × 10 ¹²	F
		B1	0.12±0.01	0.13±0.01	37.4±1.8	0.077±0.005	0.10±0.01	0.020±0.009	2.3 × 10 ¹¹	T
2008.69	54719	A0	1.77±0.09			0.000±0.005	0.00±0.01	0.054±0.008	4.5 × 10 ¹¹	F
		B1	0.05±0.01	0.15±0.01	35.2±1.7	0.085±0.006	0.12±0.01	0.020±0.012	8.5 × 10 ¹⁰	T
		A2	0.02±0.01	0.55±0.13	24.0±4.3	0.223±0.067	0.50±0.14	0.136±0.041	6.5 × 10 ⁸	F
2008.87	54786	A0	1.77±0.09			0.000±0.005	0.00±0.01	0.070±0.009	2.7 × 10 ¹¹	F
		A1	0.11±0.01	0.15±0.05	21.5±5.4	0.056±0.024	0.14±0.05	0.148±0.026	3.7 × 10 ⁹	F
2008.97	54821	A0	2.12±0.11			0.000±0.005	0.00±0.01	0.046±0.007	7.5 × 10 ¹¹	F
		B1	0.03±0.01	0.30±0.06	34.5±4.4	0.167±0.032	0.24±0.07	0.106±0.030	2.2 × 10 ⁹	F
2009.06	54855	A0	2.19±0.11			0.000±0.005	0.00±0.01	0.053±0.007	5.9 × 10 ¹¹	F
		A1	0.41±0.02	0.14±0.01	14.2±1.5	0.036±0.007	0.14±0.01	0.073±0.013	5.8 × 10 ¹⁰	F
		B1	0.03±0.01	0.39±0.18	18.9±7.8	0.128±0.093	0.37±0.19	0.263±0.047	3.7 × 10 ⁸	F
2009.14	54884	A0	1.66±0.08			0.000±0.005	0.00±0.01	0.033±0.006	1.2 × 10 ¹²	F
		B2	0.48±0.03	0.12±0.01	10.3±1.4	0.021±0.006	0.12±0.01	0.050±0.011	1.4 × 10 ¹¹	F
		B1	0.06±0.01	0.40±0.12	9.2±4.7	0.064±0.063	0.39±0.13	0.242±0.040	7.3 × 10 ⁸	F
2009.25	54922	A0	1.48±0.07			0.000±0.005	0.00±0.01	0.029±0.006	1.3 × 10 ¹²	F
		A1	0.27±0.02	0.11±0.01	15.8±1.9	0.030±0.006	0.10±0.01	0.053±0.013	7.1 × 10 ¹⁰	F
		B2	0.02±0.01	0.26±0.02	-1.7±0.8	-0.008±0.008	0.26±0.02	0.020±0.015	4.0 × 10 ¹⁰	T
		B1	0.04±0.01	0.50±0.13	8.1±3.7	0.071±0.064	0.50±0.13	0.202±0.040	7.1 × 10 ⁸	F
2009.41	54981	A0	0.45±0.02			0.000±0.005	0.00±0.01	0.043±0.010	1.9 × 10 ¹¹	F
		A1	0.16±0.01	0.10±0.02	39.3±4.5	0.061±0.010	0.07±0.02	0.080±0.018	1.8 × 10 ¹⁰	F
		B2	0.04±0.01	0.50±0.14	5.5±4.0	0.048±0.069	0.50±0.14	0.222±0.041	6.3 × 10 ⁸	F
2009.47	55003	A0	0.53±0.03			0.000±0.005	0.00±0.01	0.031±0.008	4.1 × 10 ¹¹	F
		A1	0.10±0.01	0.11±0.02	29.8±3.6	0.054±0.010	0.09±0.02	0.063±0.018	1.8 × 10 ¹⁰	F
		B2	0.03±0.01	0.57±0.21	7.9±5.4	0.078±0.104	0.56±0.21	0.269±0.049	3.2 × 10 ⁸	F
2009.56	55038	A0	0.52±0.03			0.000±0.005	0.00±0.01	0.033±0.008	3.6 × 10 ¹¹	F
		A1	0.26±0.02	0.10±0.01	43.7±2.9	0.067±0.006	0.07±0.01	0.051±0.012	7.5 × 10 ¹⁰	F
		B2	0.02±0.01	0.65±0.20	12.4±4.7	0.139±0.100	0.63±0.20	0.191±0.048	3.4 × 10 ⁸	F
2009.62	55059	A0	0.62±0.03			0.000±0.005	0.00±0.01	0.044±0.009	2.4 × 10 ¹¹	F
		A1	0.19±0.01	0.09±0.01	49.9±3.8	0.071±0.008	0.06±0.02	0.059±0.015	4.0 × 10 ¹⁰	F
		B2	0.02±0.01	0.79±0.15	10.2±2.8	0.140±0.075	0.78±0.15	0.154±0.043	5.4 × 10 ⁸	F
2009.71	55090	A0	0.81±0.04			0.000±0.005	0.00±0.01	0.049±0.009	2.5 × 10 ¹¹	F
		A1	0.26±0.02	0.10±0.01	49.0±3.5	0.078±0.008	0.07±0.02	0.071±0.015	3.8 × 10 ¹⁰	F
		A2	0.05±0.01	0.50±0.14	11.2±4.4	0.097±0.073	0.49±0.15	0.267±0.042	5.7 × 10 ⁸	F
2009.78	55118	A0	0.92±0.05			0.000±0.005	0.00±0.01	0.045±0.008	3.4 × 10 ¹¹	F
		A2	0.03±0.01	0.68±0.19	13.2±4.3	0.156±0.095	0.66±0.19	0.266±0.047	3.6 × 10 ⁸	F
2009.79	55120	A0	1.04±0.05			0.000±0.005	0.00±0.01	0.020±0.005	2.0 × 10 ¹²	T
		B3	0.26±0.02	0.09±0.01	53.2±2.9	0.072±0.005	0.05±0.01	0.030±0.009	2.3 × 10 ¹¹	F
		A2	0.04±0.01	0.61±0.18	11.6±4.5	0.123±0.089	0.59±0.18	0.283±0.046	4.0 × 10 ⁸	F
2009.80	55124	A0	1.12±0.06			0.000±0.005	0.00±0.01	0.020±0.005	2.1 × 10 ¹²	T

Table 5. Continued.

Date	MJD	Comp.	Flux (Jy)	Distance ^a (mas)	Position angle ^a (°)	Rel. RA (mas)	Rel. DEC (mas)	FWHM (mas)	T _b (K)	UL _{T_b} ^b
2009.82	55130	B3	0.30±0.02	0.09±0.01	45.4±2.9	0.067±0.006	0.07±0.01	0.049±0.012	9.3 × 10 ¹⁰	F
		A0	1.51±0.08			0.000±0.005	0.00±0.01	0.021±0.005	2.6 × 10 ¹²	F
		B3	0.19±0.01	0.13±0.02	39.5±2.9	0.086±0.009	0.10±0.02	0.077±0.016	2.4 × 10 ¹⁰	F
2009.91	55163	A2	0.04±0.01	0.67±0.17	11.2±3.7	0.132±0.084	0.66±0.17	0.241±0.045	4.5 × 10 ⁸	F
		A0	4.21±0.21			0.000±0.005	0.00±0.01	0.020±0.004	7.9 × 10 ¹²	T
		A1	0.31±0.02	0.10±0.01	34.0±2.4	0.053±0.006	0.08±0.01	0.045±0.011	1.2 × 10 ¹¹	F
2010.02	55206	B3	0.07±0.01	0.25±0.04	30.8±3.4	0.129±0.023	0.22±0.05	0.111±0.026	4.2 × 10 ⁹	F
		A2	0.01±0.01	0.52±0.02	14.1±0.7	0.126±0.011	0.50±0.02	0.020±0.018	1.6 × 10 ¹⁰	T
		A0	1.72±0.09			0.000±0.005	0.00±0.01	0.034±0.006	1.1 × 10 ¹²	F
		A1	0.34±0.02	0.08±0.01	29.5±2.9	0.038±0.006	0.07±0.01	0.047±0.011	1.2 × 10 ¹¹	F
2010.11	55238	B3	0.02±0.01	0.30±0.02	8.4±0.8	0.029±0.008	0.30±0.02	0.020±0.016	3.0 × 10 ¹⁰	T
		A2	0.03±0.01	0.52±0.30	7.2±8.5	0.066±0.152	0.52±0.30	0.386±0.057	1.7 × 10 ⁸	F
		A0	1.59±0.08			0.000±0.005	0.00±0.01	0.032±0.006	1.2 × 10 ¹²	F
		A1	0.19±0.01	0.08±0.02	26.2±3.6	0.035±0.008	0.07±0.02	0.065±0.015	3.3 × 10 ¹⁰	F
2010.18	55261	B3	0.03±0.01	0.40±0.26	8.1±9.7	0.057±0.133	0.40±0.27	0.323±0.054	2.1 × 10 ⁸	F
		A0	1.62±0.08			0.000±0.005	0.00±0.01	0.062±0.009	3.1 × 10 ¹¹	F
		A1	0.39±0.02	0.10±0.01	23.6±2.1	0.040±0.006	0.09±0.01	0.056±0.012	9.4 × 10 ¹⁰	F
2010.27	55296	B3	0.03±0.01	0.51±0.20	13.4±6.1	0.118±0.101	0.50±0.20	0.273±0.048	3.3 × 10 ⁸	F
		A0	2.95±0.15			0.000±0.005	0.00±0.01	0.034±0.006	1.9 × 10 ¹²	F
		B4	0.73±0.04	0.06±0.01	78.4±5.0	0.059±0.005	0.01±0.01	0.049±0.009	2.2 × 10 ¹¹	F
2010.38	55335	A0	1.52±0.08			0.000±0.005	0.00±0.01	0.035±0.007	9.4 × 10 ¹¹	F
		B4	0.38±0.02	0.11±0.01	59.1±3.0	0.092±0.006	0.06±0.01	0.058±0.012	8.4 × 10 ¹⁰	F
		A2	0.04±0.01	0.53±0.13	12.2±3.8	0.111±0.067	0.52±0.13	0.206±0.041	6.6 × 10 ⁸	F
2010.45	55361	A0	0.86±0.04			0.000±0.005	0.00±0.01	0.022±0.006	1.4 × 10 ¹²	F
		A1	0.28±0.02	0.06±0.01	64.1±4.9	0.050±0.005	0.02±0.01	0.022±0.008	4.5 × 10 ¹¹	F
		B4	0.18±0.01	0.14±0.01	49.7±2.7	0.108±0.008	0.09±0.02	0.063±0.015	3.4 × 10 ¹⁰	F
2010.58	55409	A0	1.12±0.06			0.000±0.005	0.00±0.01	0.020±0.005	2.1 × 10 ¹²	T
		A1	0.67±0.03	0.06±0.01	74.5±4.5	0.062±0.005	0.02±0.01	0.034±0.008	4.3 × 10 ¹¹	F
		B4	0.15±0.01	0.18±0.03	43.8±3.9	0.122±0.015	0.13±0.03	0.117±0.022	8.2 × 10 ⁹	F
2010.64	55429	A0	1.87±0.09			0.000±0.005	0.00±0.01	0.029±0.006	1.6 × 10 ¹²	F
		A1	0.41±0.02	0.09±0.01	67.3±3.8	0.083±0.006	0.03±0.01	0.063±0.012	7.7 × 10 ¹⁰	F
		A0	2.71±0.14			0.000±0.005	0.00±0.01	0.020±0.004	5.1 × 10 ¹²	T
2010.71	55457	A1	0.73±0.04	0.07±0.01	70.4±4.7	0.063±0.006	0.02±0.01	0.062±0.011	1.4 × 10 ¹¹	F
		B4	0.01±0.01	0.20±0.02	33.6±1.8	0.112±0.009	0.17±0.02	0.020±0.017	2.3 × 10 ¹⁰	T
		A2	0.06±0.01	0.57±0.16	7.1±4.1	0.070±0.080	0.56±0.16	0.310±0.044	4.9 × 10 ⁸	F
		A0	2.70±0.14			0.000±0.005	0.00±0.01	0.020±0.004	5.1 × 10 ¹²	T
2010.81	55493	A1	0.85±0.04	0.07±0.01	74.7±4.1	0.067±0.005	0.02±0.01	0.036±0.008	5.0 × 10 ¹¹	F
		A2	0.02±0.01	0.67±0.20	13.0±4.7	0.150±0.103	0.65±0.21	0.223±0.049	3.2 × 10 ⁸	F
		A0	2.44±0.12			0.000±0.005	0.00±0.01	0.036±0.006	1.4 × 10 ¹²	F
2010.84	55502	A1	0.43±0.02	0.12±0.01	83.4±3.0	0.114±0.006	0.01±0.01	0.057±0.012	9.9 × 10 ¹⁰	F
		B4	0.09±0.01	0.21±0.02	48.6±2.9	0.155±0.013	0.14±0.03	0.077±0.020	1.2 × 10 ¹⁰	F
		A2	0.03±0.01	0.66±0.28	14.7±6.9	0.167±0.146	0.64±0.29	0.324±0.056	1.8 × 10 ⁸	F
2010.85	55507	A0	2.36±0.12			0.000±0.005	0.00±0.01	0.038±0.006	1.2 × 10 ¹²	F
		A1	0.22±0.01	0.14±0.01	69.0±4.3	0.131±0.011	0.05±0.02	0.100±0.018	1.6 × 10 ¹⁰	F
2010.87	55513	A0	2.08±0.10			0.000±0.005	0.00±0.01	0.023±0.005	3.0 × 10 ¹²	F
		A1	0.20±0.01	0.14±0.01	69.5±3.6	0.133±0.009	0.05±0.02	0.081±0.017	2.3 × 10 ¹⁰	F

Table 5. Continued.

Date	MJD	Comp.	Flux (Jy)	Distance ^a (mas)	Position angle ^a ($^{\circ}$)	Rel. RA (mas)	Rel. DEC (mas)	FWHM (mas)	T _b (K)	UL _{T_b} ^b
2010.92	55534	B4	0.03±0.01	0.28±0.13	31.1±10.4	0.142±0.075	0.24±0.15	0.207±0.043	5.4 × 10 ⁸	F
		A2	0.01±0.01	0.68±0.35	14.8±8.3	0.175±0.181	0.66±0.36	0.294±0.062	1.2 × 10 ⁸	F
		A0	1.56±0.08			0.000±0.005	0.00±0.01	0.020±0.005	2.9 × 10 ¹²	T
		A1	0.05±0.01	0.19±0.01	61.2±1.7	0.166±0.006	0.09±0.01	0.020±0.012	9.2 × 10 ¹⁰	T
2011.00	55563	B4	0.01±0.01	0.44±0.22	21.9±9.1	0.163±0.117	0.41±0.23	0.207±0.051	2.6 × 10 ⁸	F
		A0	1.40±0.07			0.000±0.005	0.00±0.01	0.025±0.006	1.6 × 10 ¹²	F
		B5	0.59±0.03	0.12±0.01	61.4±2.8	0.101±0.006	0.06±0.01	0.073±0.012	8.2 × 10 ¹⁰	F
2011.10	55597	A2	0.02±0.02	0.68±0.49	14.8±11.6	0.174±0.252	0.66±0.50	0.470±0.071	7.2 × 10 ⁷	F
		A0	0.88±0.04			0.000±0.005	0.00±0.01	0.020±0.006	1.7 × 10 ¹²	T
		B5	0.29±0.02	0.18±0.01	51.9±2.3	0.144±0.009	0.11±0.02	0.090±0.016	2.6 × 10 ¹⁰	F
2011.16	55621	A0	1.11±0.06			0.000±0.005	0.00±0.01	0.020±0.005	2.1 × 10 ¹²	T
		B5	0.09±0.01	0.25±0.03	47.5±3.3	0.187±0.018	0.17±0.04	0.106±0.023	6.1 × 10 ⁹	F
2011.30	55672	A0	1.72±0.09			0.000±0.005	0.00±0.01	0.020±0.005	3.2 × 10 ¹²	T
		A1	0.39±0.02	0.10±0.01	36.7±2.3	0.061±0.006	0.08±0.01	0.050±0.011	1.2 × 10 ¹¹	F
		B5	0.20±0.01	0.33±0.03	40.8±2.5	0.216±0.019	0.25±0.04	0.167±0.024	5.4 × 10 ⁹	F
2011.39	55703	A0	2.77±0.14			0.000±0.005	0.00±0.01	0.038±0.006	1.4 × 10 ¹²	F
		B5	0.30±0.02	0.37±0.05	30.7±2.8	0.187±0.026	0.31±0.05	0.267±0.027	3.2 × 10 ⁹	F
		A0	2.84±0.14			0.000±0.005	0.00±0.01	0.055±0.007	7.0 × 10 ¹¹	F
2011.44	55724	B5	0.17±0.01	0.43±0.04	30.6±2.1	0.219±0.024	0.37±0.05	0.187±0.026	3.7 × 10 ⁹	F
		A0	2.68±0.13			0.000±0.005	0.00±0.01	0.020±0.004	5.0 × 10 ¹²	T
		B5	0.15±0.01	0.56±0.07	28.9±2.6	0.272±0.039	0.49±0.08	0.257±0.032	1.6 × 10 ⁹	F
2011.64	55796	A2	0.10±0.01	0.66±0.09	28.0±2.8	0.308±0.050	0.58±0.10	0.262±0.036	1.1 × 10 ⁹	F
		A0	2.30±0.12			0.000±0.005	0.00±0.01	0.020±0.005	4.3 × 10 ¹²	F
		A1	0.46±0.02	0.08±0.01	45.5±2.9	0.060±0.005	0.06±0.01	0.039±0.009	2.3 × 10 ¹¹	F
		A2	0.03±0.01	0.60±0.07	31.6±2.4	0.313±0.036	0.51±0.07	0.103±0.031	1.8 × 10 ⁹	F
2011.71	55820	B5	0.08±0.01	0.76±0.15	27.3±3.9	0.348±0.081	0.68±0.16	0.343±0.044	4.8 × 10 ⁸	F
		A0	2.08±0.10			0.000±0.005	0.00±0.01	0.037±0.006	1.1 × 10 ¹²	F
		A1	0.19±0.01	0.14±0.01	39.6±2.1	0.091±0.007	0.11±0.01	0.052±0.014	5.1 × 10 ¹⁰	F
		A2	0.03±0.01	0.51±0.12	33.7±5.2	0.280±0.066	0.42±0.13	0.187±0.040	6.6 × 10 ⁸	F
2011.72	55824	B5	0.04±0.01	0.81±0.18	27.8±4.5	0.379±0.100	0.72±0.20	0.289±0.048	3.3 × 10 ⁸	F
		A0	1.84±0.09			0.000±0.005	0.00±0.01	0.020±0.005	3.4 × 10 ¹²	T
		A1	0.59±0.03	0.07±0.01	47.1±3.5	0.054±0.005	0.05±0.01	0.048±0.010	1.9 × 10 ¹¹	F
		B5	0.07±0.01	0.80±0.12	29.0±3.0	0.388±0.065	0.70±0.13	0.281±0.040	6.9 × 10 ⁸	F
2011.75	55833	A0	2.44±0.12			0.000±0.005	0.00±0.01	0.057±0.008	5.6 × 10 ¹¹	F
		A1	0.20±0.01	0.14±0.01	46.9±2.2	0.099±0.006	0.09±0.01	0.046±0.013	7.1 × 10 ¹⁰	F
		A0	1.96±0.10			0.000±0.005	0.00±0.01	0.055±0.008	4.9 × 10 ¹¹	F
2011.79	55850	A1	0.17±0.01	0.16±0.02	39.2±3.3	0.098±0.012	0.12±0.02	0.099±0.019	1.3 × 10 ¹⁰	F
		B5	0.05±0.01	0.83±0.19	27.3±4.6	0.381±0.104	0.74±0.21	0.355±0.049	3.2 × 10 ⁸	F
		A0	2.47±0.12			0.000±0.005	0.00±0.01	0.040±0.006	1.2 × 10 ¹²	F
		B6	0.31±0.02	0.11±0.01	34.2±2.3	0.063±0.006	0.09±0.01	0.058±0.013	6.8 × 10 ¹⁰	F
2011.92	55897	B5	0.02±0.01	0.89±0.27	26.8±6.0	0.403±0.147	0.80±0.29	0.320±0.056	1.8 × 10 ⁸	F
		A0	0.63±0.03			0.000±0.005	0.00±0.01	0.032±0.008	4.6 × 10 ¹¹	F
		A1	0.15±0.01	0.11±0.02	42.2±4.0	0.074±0.010	0.08±0.02	0.076±0.017	2.0 × 10 ¹⁰	F
2012.07	55953	B6	0.04±0.01	0.34±0.06	23.6±3.3	0.136±0.032	0.31±0.06	0.118±0.030	2.2 × 10 ⁹	F
		A0	0.97±0.05			0.000±0.005	0.00±0.01	0.037±0.008	5.3 × 10 ¹¹	F
		A1	0.39±0.02	0.09±0.01	42.0±3.0	0.060±0.006	0.07±0.01	0.057±0.012	9.0 × 10 ¹⁰	F

Table 5. Continued.

Date	MJD	Comp.	Flux (Jy)	Distance ^a (mas)	Position angle ^a (°)	Rel. RA (mas)	Rel. DEC (mas)	FWHM (mas)	T _b (K)	UL _{T_b} ^b
2012.25	56019	B6	0.02±0.01	0.48±0.19	25.9±7.6	0.210±0.102	0.43±0.20	0.223±0.048	3.3 × 10 ⁸	F
		B5	0.03±0.01	0.94±0.30	24.5±6.0	0.388±0.159	0.85±0.32	0.363±0.058	1.5 × 10 ⁸	F
		A0	1.34±0.07			0.000±0.005	0.00±0.01	0.027±0.006	1.4 × 10 ¹²	F
2012.29	56033	A1	0.63±0.03	0.10±0.01	40.5±3.1	0.064±0.007	0.07±0.01	0.096±0.014	5.2 × 10 ¹⁰	F
		B6	0.02±0.01	0.54±0.15	24.8±5.3	0.227±0.080	0.49±0.16	0.180±0.044	4.8 × 10 ⁸	F
		A0	0.80±0.04			0.000±0.005	0.00±0.01	0.020±0.006	1.5 × 10 ¹²	T
2012.30	56037	A1	0.40±0.02	0.13±0.01	38.5±2.3	0.078±0.007	0.10±0.01	0.074±0.013	5.4 × 10 ¹⁰	F
		A0	0.54±0.03			0.000±0.005	0.00±0.01	0.020±0.006	1.0 × 10 ¹²	T
		A1	0.32±0.02	0.11±0.01	38.6±2.5	0.071±0.007	0.09±0.01	0.067±0.014	5.3 × 10 ¹⁰	F
2012.32	56045	A0	0.41±0.02			0.000±0.005	0.00±0.01	0.033±0.009	2.8 × 10 ¹¹	F
		A1	0.23±0.02	0.15±0.03	41.5±4.8	0.100±0.017	0.11±0.03	0.156±0.022	7.1 × 10 ⁹	F
		B6	0.01±0.01	0.66±0.15	26.2±4.5	0.290±0.082	0.59±0.16	0.144±0.044	4.7 × 10 ⁸	F
2012.40	56073	A0	0.46±0.02			0.000±0.005	0.00±0.01	0.023±0.007	6.6 × 10 ¹¹	F
		B7	0.14±0.01	0.11±0.01	31.7±2.6	0.060±0.008	0.10±0.02	0.055±0.015	3.6 × 10 ¹⁰	F
		B6	0.02±0.01	0.65±0.21	29.4±6.7	0.317±0.115	0.56±0.23	0.231±0.051	2.6 × 10 ⁸	F
2012.51	56113	A0	0.66±0.03			0.000±0.005	0.00±0.01	0.020±0.006	1.2 × 10 ¹²	T
		B7	0.18±0.01	0.12±0.01	31.4±2.5	0.064±0.008	0.10±0.02	0.061±0.015	3.7 × 10 ¹⁰	F
		B6	0.03±0.01	0.80±0.23	25.6±5.5	0.347±0.123	0.72±0.25	0.297±0.052	2.4 × 10 ⁸	F
2012.62	56153	A0	0.74±0.04			0.000±0.005	0.00±0.01	0.020±0.006	1.4 × 10 ¹²	T
		B7	0.06±0.01	0.16±0.03	24.3±4.0	0.066±0.018	0.15±0.04	0.085±0.023	5.9 × 10 ⁹	F
		B6	0.01±0.01	0.92±0.14	24.7±3.0	0.385±0.077	0.84±0.16	0.138±0.043	5.1 × 10 ⁸	F
2012.77	56208	A0	2.06±0.10			0.000±0.005	0.00±0.01	0.038±0.006	1.1 × 10 ¹²	F
		B7	0.12±0.01	0.19±0.03	5.4±2.5	0.008±0.016	0.19±0.03	0.112±0.022	7.3 × 10 ⁹	F
		A0	2.60±0.13			0.000±0.005	0.00±0.01	0.062±0.008	5.1 × 10 ¹¹	F
2012.80	56220	B7	0.03±0.01	0.21±0.13	-0.5±8.6	-0.002±0.064	0.21±0.13	0.190±0.040	7.1 × 10 ⁸	F
		A0	3.78±0.19			0.000±0.005	0.00±0.01	0.067±0.007	6.3 × 10 ¹¹	F
		B7	0.04±0.01	0.27±0.05	-10.8±2.7	-0.050±0.024	0.26±0.05	0.090±0.026	3.7 × 10 ⁹	F
2012.82	56228	A2	0.08±0.01	0.61±0.10	30.4±3.4	0.309±0.055	0.53±0.11	0.257±0.037	9.2 × 10 ⁸	F
		A0	3.23±0.16			0.000±0.005	0.00±0.01	0.055±0.007	8.0 × 10 ¹¹	F
		B8	0.87±0.04	0.05±0.01	31.1±4.6	0.024±0.005	0.04±0.01	0.054±0.009	2.2 × 10 ¹¹	F
2012.83	56229	B7	0.02±0.01	0.21±0.02	-6.7±1.1	-0.024±0.008	0.21±0.02	0.020±0.015	3.9 × 10 ¹⁰	T
		A2	0.09±0.01	0.61±0.22	23.4±6.7	0.240±0.117	0.56±0.23	0.520±0.051	2.6 × 10 ⁸	F
		A0	2.88±0.14			0.000±0.005	0.00±0.01	0.029±0.005	2.6 × 10 ¹²	F
2012.97	56283	B8	0.85±0.04	0.12±0.01	44.6±2.0	0.087±0.005	0.09±0.01	0.055±0.010	2.1 × 10 ¹¹	F
		B7	0.02±0.01	0.28±0.06	24.1±3.9	0.115±0.031	0.26±0.06	0.077±0.029	2.4 × 10 ⁹	F
		A2	0.17±0.01	0.51±0.09	36.5±4.0	0.302±0.050	0.41±0.10	0.343±0.036	1.1 × 10 ⁹	F
2013.04	56307	A0	3.62±0.18			0.000±0.005	0.00±0.01	0.021±0.004	6.2 × 10 ¹²	F
		A1	0.67±0.03	0.10±0.01	39.1±2.3	0.060±0.005	0.07±0.01	0.033±0.008	4.6 × 10 ¹¹	F
		B8	0.48±0.03	0.20±0.01	35.0±1.5	0.115±0.007	0.16±0.01	0.088±0.014	4.7 × 10 ¹⁰	F
2013.15	56349	B7	0.11±0.01	0.42±0.10	24.1±4.5	0.172±0.054	0.38±0.11	0.297±0.037	9.4 × 10 ⁸	F
		A0	1.79±0.09			0.000±0.005	0.00±0.01	0.020±0.005	3.4 × 10 ¹²	T
		A1	0.47±0.03	0.13±0.01	38.2±1.9	0.077±0.006	0.10±0.01	0.051±0.011	1.4 × 10 ¹¹	F
2013.29	56398	B8	0.13±0.01	0.42±0.04	29.0±1.9	0.202±0.021	0.36±0.04	0.145±0.025	4.6 × 10 ⁹	F
		B7	0.08±0.01	0.77±0.12	31.5±3.5	0.399±0.070	0.65±0.14	0.303±0.041	6.1 × 10 ⁸	F
		A0	0.73±0.04			0.000±0.005	0.00±0.01	0.020±0.006	1.4 × 10 ¹²	F
		A1	0.12±0.01	0.11±0.01	39.5±2.9	0.071±0.008	0.09±0.02	0.048±0.015	3.8 × 10 ¹⁰	F

Table 5. Continued.

Date	MJD	Comp.	Flux (Jy)	Distance ^a (mas)	Position angle ^a ($^{\circ}$)	Rel. RA (mas)	Rel. DEC (mas)	FWHM (mas)	T _b (K)	UL _{T_b} ^b
2013.41	56442	B8	0.09±0.01	0.53±0.06	29.1±2.2	0.255±0.031	0.46±0.06	0.165±0.029	2.4 × 10 ⁹	F
		B7	0.07±0.01	0.96±0.10	30.6±2.2	0.490±0.055	0.83±0.11	0.233±0.037	9.1 × 10 ⁸	F
		A0	1.26±0.06			0.000±0.005	0.00±0.01	0.032±0.007	9.3 × 10 ¹¹	F
		A1	0.11±0.01	0.08±0.01	64.9±6.3	0.073±0.010	0.03±0.02	0.062±0.017	2.1 × 10 ¹⁰	F
2013.49	56473	B8	0.03±0.01	0.81±0.22	30.9±5.9	0.415±0.123	0.69±0.25	0.329±0.052	2.4 × 10 ⁸	F
		B7	0.03±0.01	1.10±0.32	24.3±5.4	0.454±0.170	1.01±0.34	0.417±0.060	1.4 × 10 ⁸	F
		A0	3.37±0.17			0.000±0.005	0.00±0.01	0.020±0.004	6.3 × 10 ¹²	T
		A1	0.71±0.04	0.10±0.01	42.0±2.8	0.068±0.006	0.08±0.01	0.086±0.013	7.2 × 10 ¹⁰	F
2013.57	56501	B8	0.03±0.01	0.82±0.23	29.8±6.0	0.405±0.129	0.71±0.26	0.327±0.054	2.2 × 10 ⁸	F
		B7	0.02±0.01	1.22±0.28	24.4±4.3	0.504±0.148	1.11±0.30	0.254±0.057	1.7 × 10 ⁸	F
		A0	2.95±0.15			0.000±0.005	0.00±0.01	0.024±0.005	3.8 × 10 ¹²	F
		A1	0.88±0.04	0.07±0.01	19.5±2.5	0.023±0.005	0.06±0.01	0.020±0.006	1.7 × 10 ¹²	T
2013.65	56530	B9	0.67±0.04	0.14±0.02	15.4±1.7	0.037±0.008	0.14±0.02	0.117±0.015	3.7 × 10 ¹⁰	F
		A0	2.20±0.11			0.000±0.005	0.00±0.01	0.027±0.005	2.3 × 10 ¹²	F
		A1	0.26±0.02	0.10±0.01	23.6±2.6	0.042±0.008	0.10±0.02	0.070±0.015	3.9 × 10 ¹⁰	F
2013.88	56614	B9	0.09±0.01	0.31±0.09	25.4±5.5	0.134±0.048	0.28±0.10	0.238±0.035	1.2 × 10 ⁹	F
		A0	2.53±0.13			0.000±0.005	0.00±0.01	0.041±0.006	1.1 × 10 ¹²	F
		A1	0.35±0.02	0.15±0.01	24.6±1.4	0.062±0.006	0.14±0.01	0.052±0.012	9.7 × 10 ¹⁰	F
2013.96	56642	B9	0.13±0.01	0.39±0.05	6.3±1.9	0.042±0.026	0.38±0.05	0.172±0.027	3.3 × 10 ⁹	F
		A0	1.80±0.09			0.000±0.005	0.00±0.01	0.045±0.007	6.7 × 10 ¹¹	F
		A1	0.19±0.01	0.12±0.01	39.7±2.3	0.078±0.007	0.10±0.01	0.047±0.013	6.6 × 10 ¹⁰	F
2014.05	56677	B9	0.10±0.01	0.51±0.10	7.2±3.0	0.064±0.052	0.51±0.11	0.270±0.037	9.9 × 10 ⁸	F
		A0	1.21±0.06			0.000±0.005	0.00±0.01	0.043±0.008	4.9 × 10 ¹¹	F
		A1	0.13±0.01	0.07±0.01	62.7±3.8	0.066±0.005	0.03±0.01	0.020±0.009	2.5 × 10 ¹¹	T
2014.15	56712	B9	0.06±0.01	0.62±0.17	10.8±4.1	0.116±0.083	0.61±0.17	0.323±0.045	4.5 × 10 ⁸	F
		A0	1.51±0.08			0.000±0.005	0.00±0.01	0.054±0.008	3.9 × 10 ¹¹	F
		A1	0.15±0.01	0.12±0.01	56.6±2.2	0.103±0.005	0.07±0.01	0.020±0.009	2.9 × 10 ¹¹	T
2014.33	56780	B9	0.09±0.01	0.72±0.25	19.6±6.0	0.240±0.130	0.67±0.26	0.559±0.054	2.2 × 10 ⁸	F
		A0	1.90±0.10			0.000±0.005	0.00±0.01	0.038±0.007	9.9 × 10 ¹¹	F
		A1	0.33±0.02	0.13±0.01	32.7±2.0	0.071±0.007	0.11±0.01	0.064±0.013	6.1 × 10 ¹⁰	F
2014.47	56828	A0	1.98±0.10			0.000±0.005	0.00±0.01	0.060±0.008	4.1 × 10 ¹¹	F
		A1	0.20±0.02	0.15±0.07	21.0±8.4	0.055±0.039	0.14±0.08	0.300±0.032	1.6 × 10 ⁹	F
2014.57	56866	A0	1.62±0.08			0.000±0.005	0.00±0.01	0.020±0.005	3.0 × 10 ¹²	F
		A1	0.57±0.03	0.09±0.01	86.1±3.2	0.093±0.005	0.01±0.01	0.034±0.008	3.7 × 10 ¹¹	F
		B10	0.09±0.01	0.16±0.03	52.0±5.6	0.129±0.019	0.10±0.04	0.107±0.024	5.8 × 10 ⁹	F
2014.73	56923	A0	1.32±0.07			0.000±0.005	0.00±0.01	0.020±0.005	2.5 × 10 ¹²	F
		A1	0.21±0.01	0.10±0.01	77.6±3.2	0.095±0.006	0.02±0.01	0.031±0.010	1.6 × 10 ¹¹	F
		B10	0.24±0.02	0.19±0.01	69.1±2.8	0.174±0.010	0.07±0.02	0.093±0.017	2.1 × 10 ¹⁰	F
2014.87	56976	A2	0.03±0.01	0.48±0.12	19.1±4.4	0.158±0.065	0.46±0.13	0.189±0.040	6.9 × 10 ⁸	F
		A0	2.66±0.13			0.000±0.005	0.00±0.01	0.020±0.004	5.0 × 10 ¹²	T
		A1	0.05±0.01	0.12±0.01	66.1±2.6	0.113±0.006	0.05±0.01	0.020±0.012	9.8 × 10 ¹⁰	T
2014.93	56996	B10	0.27±0.02	0.21±0.02	61.4±2.8	0.186±0.011	0.10±0.02	0.116±0.019	1.5 × 10 ¹⁰	F
		A0	1.71±0.09			0.000±0.005	0.00±0.01	0.020±0.005	3.2 × 10 ¹²	T
		A1	0.57±0.03	0.09±0.01	55.2±2.8	0.077±0.005	0.05±0.01	0.038±0.009	3.0 × 10 ¹¹	F
2014.99	57020	B10	0.20±0.01	0.25±0.02	55.2±2.4	0.204±0.012	0.14±0.02	0.105±0.019	1.3 × 10 ¹⁰	F
		A0	1.17±0.06			0.000±0.005	0.00±0.01	0.020±0.005	2.2 × 10 ¹²	T

Table 5. Continued.

Date	MJD	Comp.	Flux (Jy)	Distance ^a (mas)	Position angle ^a (°)	Rel. RA (mas)	Rel. DEC (mas)	FWHM (mas)	T _b (K)	UL _{T_b} ^b
2015.12	57068	A1	0.17±0.01	0.12±0.01	50.8±2.2	0.092±0.005	0.08±0.01	0.025±0.010	2.0 × 10 ¹¹	F
		B10	0.26±0.02	0.31±0.02	54.0±2.2	0.249±0.014	0.18±0.03	0.138±0.021	1.0 × 10 ¹⁰	F
		A0	1.98±0.10			0.000±0.005	0.00±0.01	0.020±0.005	3.7 × 10 ¹²	T
2015.27	57123	A1	0.25±0.01	0.15±0.01	51.2±2.2	0.115±0.007	0.09±0.01	0.055±0.013	6.1 × 10 ¹⁰	F
		B10	0.14±0.01	0.35±0.06	41.0±4.6	0.229±0.037	0.26±0.07	0.241±0.032	1.8 × 10 ⁹	F
		A0	2.09±0.11			0.000±0.005	0.00±0.01	0.020±0.005	3.9 × 10 ¹²	T
2015.36	57153	A1	0.37±0.02	0.09±0.01	51.3±3.3	0.069±0.006	0.06±0.01	0.057±0.012	8.6 × 10 ¹⁰	F
		B10	0.09±0.01	0.48±0.06	36.3±2.9	0.287±0.034	0.39±0.07	0.179±0.030	2.1 × 10 ⁹	F
		A0	1.58±0.08			0.000±0.005	0.00±0.01	0.023±0.005	2.2 × 10 ¹²	F
2015.44	57182	A1	0.31±0.02	0.10±0.01	48.7±3.2	0.074±0.007	0.07±0.01	0.063±0.013	5.8 × 10 ¹⁰	F
		B10	0.07±0.01	0.50±0.08	35.1±3.6	0.286±0.045	0.41±0.09	0.201±0.034	1.3 × 10 ⁹	F
		A0	0.95±0.05			0.000±0.005	0.00±0.01	0.020±0.006	1.8 × 10 ¹²	T
2015.50	57205	A1	0.31±0.02	0.14±0.01	47.5±2.3	0.106±0.007	0.10±0.01	0.067±0.014	5.1 × 10 ¹⁰	F
		B10	0.05±0.01	0.54±0.08	36.2±3.6	0.320±0.048	0.44±0.10	0.189±0.035	1.1 × 10 ⁹	F
		A0	1.66±0.08			0.000±0.005	0.00±0.01	0.020±0.005	3.1 × 10 ¹²	F
2015.58	57235	A1	0.21±0.01	0.10±0.01	31.6±2.9	0.052±0.008	0.08±0.02	0.062±0.014	4.1 × 10 ¹⁰	F
		B10	0.07±0.01	0.50±0.06	39.8±2.9	0.321±0.034	0.39±0.07	0.158±0.030	2.1 × 10 ⁹	F
		A0	1.90±0.10			0.000±0.005	0.00±0.01	0.020±0.005	3.6 × 10 ¹²	F
2015.72	57287	A1	0.41±0.02	0.12±0.01	30.0±1.9	0.062±0.006	0.11±0.01	0.061±0.012	8.3 × 10 ¹⁰	F
		B10	0.05±0.01	0.55±0.12	37.7±5.6	0.333±0.073	0.43±0.15	0.243±0.042	5.7 × 10 ⁸	F
		A0	2.51±0.13			0.000±0.005	0.00±0.01	0.020±0.004	4.7 × 10 ¹²	T
2015.93	57361	A1	0.19±0.01	0.15±0.02	36.7±2.4	0.089±0.009	0.12±0.02	0.073±0.016	2.6 × 10 ¹⁰	F
		A2	0.07±0.01	0.45±0.07	30.3±3.4	0.228±0.041	0.39±0.08	0.184±0.033	1.5 × 10 ⁹	F
		B10	0.11±0.01	0.64±0.06	36.6±2.4	0.379±0.037	0.51±0.07	0.211±0.032	1.8 × 10 ⁹	F
2016.00	57388	A0	1.62±0.08			0.000±0.005	0.00±0.01	0.020±0.005	3.0 × 10 ¹²	T
		A1	0.11±0.01	0.18±0.02	26.7±2.1	0.083±0.011	0.16±0.02	0.072±0.018	1.6 × 10 ¹⁰	F
		A2	0.02±0.01	0.55±0.18	29.5±6.9	0.269±0.100	0.48±0.20	0.195±0.048	3.4 × 10 ⁸	F
2016.08	57419	B10	0.07±0.01	0.87±0.10	32.7±2.7	0.469±0.059	0.73±0.12	0.255±0.039	8.1 × 10 ⁸	F
		A0	0.84±0.04			0.000±0.005	0.00±0.01	0.020±0.006	1.6 × 10 ¹²	T
		A1	0.08±0.01	0.15±0.04	18.2±4.1	0.047±0.019	0.14±0.04	0.100±0.024	5.8 × 10 ⁹	F
2016.21	57465	A2	0.02±0.01	0.47±0.19	31.1±8.8	0.241±0.107	0.40±0.21	0.212±0.049	3.0 × 10 ⁸	F
		B10	0.06±0.01	0.91±0.16	32.4±3.8	0.489±0.090	0.77±0.18	0.326±0.046	4.0 × 10 ⁸	F
		A0	1.42±0.07			0.000±0.005	0.00±0.01	0.020±0.005	2.7 × 10 ¹²	T
2016.31	57500	A1	0.16±0.01	0.11±0.02	6.2±2.5	0.012±0.010	0.11±0.02	0.075±0.017	2.1 × 10 ¹⁰	F
		A2	0.02±0.01	0.43±0.15	29.1±7.3	0.210±0.084	0.38±0.17	0.197±0.045	4.4 × 10 ⁸	F
		B10	0.05±0.01	0.92±0.14	31.3±3.3	0.475±0.078	0.78±0.16	0.270±0.043	5.0 × 10 ⁸	F
2016.44	57549	A0	0.73±0.04			0.000±0.005	0.00±0.01	0.030±0.007	6.1 × 10 ¹¹	F
		A1	0.06±0.01	0.13±0.04	10.3±4.2	0.023±0.018	0.13±0.04	0.085±0.023	6.0 × 10 ⁹	F
		A2	0.02±0.01	0.38±0.12	14.5±5.0	0.096±0.061	0.37±0.12	0.143±0.039	7.7 × 10 ⁸	F
2016.31	57500	B10	0.02±0.01	0.99±0.33	28.6±6.8	0.472±0.180	0.87±0.36	0.379±0.061	1.3 × 10 ⁸	F
		A0	2.96±0.15			0.000±0.005	0.00±0.01	0.020±0.004	5.5 × 10 ¹²	T
		A1	0.38±0.02	0.07±0.01	18.7±2.6	0.022±0.006	0.07±0.01	0.046±0.011	1.3 × 10 ¹¹	F
2016.44	57549	A2	0.04±0.01	0.46±0.17	17.6±6.0	0.140±0.086	0.44±0.17	0.277±0.045	4.3 × 10 ⁸	F
		B10	0.03±0.01	0.92±0.22	29.8±4.9	0.456±0.120	0.80±0.24	0.276±0.052	2.5 × 10 ⁸	F
		A0	1.83±0.09			0.000±0.005	0.00±0.01	0.020±0.005	3.4 × 10 ¹²	F
		A1	0.19±0.01	0.13±0.02	17.8±1.9	0.039±0.008	0.12±0.02	0.060±0.015	4.0 × 10 ¹⁰	F

Table 5. Continued.

Date	MJD	Comp.	Flux (Jy)	Distance ^a (mas)	Position angle ^a ($^{\circ}$)	Rel. RA (mas)	Rel. DEC (mas)	FWHM (mas)	T _b (K)	UL _{T_b} ^b
2016.51	57573	A2	0.03±0.01	0.49±0.12	10.7±3.7	0.090±0.059	0.48±0.12	0.173±0.039	8.0 × 10 ⁸	F
		B10	0.02±0.01	1.04±0.28	30.9±5.8	0.535±0.158	0.89±0.32	0.295±0.058	1.6 × 10 ⁸	F
		A0	1.16±0.06			0.000±0.005	0.00±0.01	0.023±0.006	1.7 × 10 ¹²	F
		A1	0.18±0.01	0.10±0.02	30.4±3.5	0.049±0.009	0.08±0.02	0.073±0.016	2.5 × 10 ¹⁰	F
2016.58	57600	A2	0.04±0.01	0.44±0.16	13.1±5.8	0.099±0.083	0.43±0.17	0.268±0.044	4.6 × 10 ⁸	F
		A0	1.67±0.08			0.000±0.005	0.00±0.01	0.032±0.006	1.2 × 10 ¹²	F
		A1	0.23±0.01	0.12±0.02	13.6±2.5	0.029±0.010	0.12±0.02	0.093±0.017	2.0 × 10 ¹⁰	F
2016.68	57636	A2	0.07±0.01	0.49±0.16	14.3±5.2	0.121±0.082	0.48±0.17	0.335±0.044	4.6 × 10 ⁸	F
		A0	1.70±0.09			0.000±0.005	0.00±0.01	0.026±0.006	1.9 × 10 ¹²	F
		A1	0.22±0.01	0.15±0.01	14.6±1.5	0.037±0.007	0.14±0.01	0.055±0.014	5.4 × 10 ¹⁰	F
2016.76	57667	A2	0.03±0.01	0.47±0.17	10.3±5.3	0.085±0.084	0.47±0.17	0.224±0.045	4.5 × 10 ⁸	F
		A0	1.60±0.08			0.000±0.005	0.00±0.01	0.024±0.005	2.1 × 10 ¹²	F
		A1	0.18±0.01	0.11±0.02	20.5±2.6	0.037±0.008	0.10±0.02	0.067±0.016	3.0 × 10 ¹⁰	F
2016.81	57684	A2	0.08±0.01	0.49±0.06	11.6±2.0	0.098±0.032	0.48±0.06	0.160±0.030	2.3 × 10 ⁹	F
		A0	1.48±0.07			0.000±0.005	0.00±0.01	0.029±0.006	1.3 × 10 ¹²	F
		A1	0.21±0.01	0.13±0.02	19.3±2.3	0.042±0.009	0.12±0.02	0.078±0.016	2.6 × 10 ¹⁰	F
2016.91	57720	A2	0.06±0.01	0.56±0.11	12.5±3.0	0.120±0.056	0.55±0.11	0.230±0.038	8.9 × 10 ⁸	F
		A0	2.47±0.12			0.000±0.005	0.00±0.01	0.020±0.004	4.6 × 10 ¹²	F
		A1	0.16±0.01	0.06±0.01	41.0±4.7	0.042±0.007	0.05±0.01	0.048±0.014	5.2 × 10 ¹⁰	F
2016.98	57746	B11	0.08±0.01	0.19±0.03	11.4±2.7	0.037±0.017	0.18±0.03	0.092±0.022	7.3 × 10 ⁹	F
		A2	0.02±0.01	0.51±0.23	14.4±7.3	0.126±0.118	0.49±0.24	0.244±0.052	2.5 × 10 ⁸	F
		A0	1.32±0.07			0.000±0.005	0.00±0.01	0.033±0.007	9.1 × 10 ¹¹	F
		A1	0.35±0.02	0.11±0.01	21.3±2.2	0.039±0.007	0.10±0.01	0.067±0.013	5.8 × 10 ¹⁰	F
2017.04	57767	B11	0.03±0.01	0.29±0.06	-3.4±2.8	-0.017±0.028	0.29±0.06	0.085±0.028	2.8 × 10 ⁹	F
		A2	0.06±0.01	0.48±0.09	13.5±2.8	0.112±0.043	0.47±0.09	0.183±0.034	1.4 × 10 ⁹	F
		A0	0.73±0.04			0.000±0.005	0.00±0.01	0.020±0.006	1.4 × 10 ¹²	T
		A1	0.12±0.01	0.16±0.02	17.6±2.0	0.048±0.010	0.15±0.02	0.065±0.017	2.0 × 10 ¹⁰	F
2017.10	57789	B11	0.01±0.01	0.32±0.03	9.0±1.2	0.050±0.013	0.32±0.03	0.020±0.020	1.1 × 10 ¹⁰	T
		A2	0.05±0.01	0.52±0.09	11.0±2.6	0.099±0.044	0.51±0.09	0.171±0.034	1.3 × 10 ⁹	F
		A0	0.83±0.04			0.000±0.005	0.00±0.01	0.020±0.006	1.6 × 10 ¹²	T
		A1	0.12±0.01	0.13±0.02	26.2±3.1	0.057±0.011	0.12±0.02	0.076±0.018	1.6 × 10 ¹⁰	F
2017.21	57831	B11	0.02±0.01	0.39±0.09	9.9±3.4	0.066±0.043	0.38±0.09	0.091±0.034	1.4 × 10 ⁹	F
		A2	0.04±0.01	0.60±0.12	12.5±3.2	0.130±0.062	0.59±0.12	0.211±0.039	7.4 × 10 ⁸	F
		A0	0.85±0.04			0.000±0.005	0.00±0.01	0.020±0.006	1.6 × 10 ¹²	F
		A1	0.03±0.01	0.15±0.04	26.3±5.2	0.066±0.021	0.13±0.04	0.065±0.025	4.6 × 10 ⁹	F
2017.29	57859	A2	0.01±0.01	0.62±0.24	16.0±6.4	0.171±0.125	0.60±0.25	0.189±0.053	2.3 × 10 ⁸	F
		A0	1.44±0.07			0.000±0.005	0.00±0.01	0.033±0.007	9.9 × 10 ¹¹	F
		A1	0.09±0.01	0.13±0.01	73.3±2.4	0.123±0.006	0.04±0.01	0.020±0.010	1.7 × 10 ¹¹	T
2017.36	57886	A0	1.81±0.09			0.000±0.005	0.00±0.01	0.036±0.006	1.0 × 10 ¹²	F
2017.43	57912	A1	0.41±0.02	0.10±0.01	-4.9±1.9	-0.009±0.007	0.10±0.01	0.071±0.013	6.1 × 10 ¹⁰	F
		A0	3.66±0.18			0.000±0.005	0.00±0.01	0.020±0.004	6.9 × 10 ¹²	T
2017.50	57937	A1	0.97±0.05	0.06±0.02	0.6±4.1	0.001±0.009	0.06±0.02	0.159±0.016	2.9 × 10 ¹⁰	F
		A0	4.04±0.20			0.000±0.005	0.00±0.01	0.080±0.008	4.7 × 10 ¹¹	F
2017.59	57971	A0	6.08±0.30			0.000±0.005	0.00±0.01	0.084±0.007	6.5 × 10 ¹¹	F
		A1	0.09±0.01	0.13±0.01	73.3±2.4	0.123±0.006	0.04±0.01	0.020±0.010	1.7 × 10 ¹¹	T
		A2	0.05±0.01	0.56±0.07	14.5±2.1	0.140±0.037	0.54±0.07	0.149±0.032	1.8 × 10 ⁹	F
2017.67	58000	A0	3.13±0.16			0.000±0.005	0.00±0.01	0.028±0.005	3.0 × 10 ¹²	F

Table 5. Continued.

Date	MJD	Comp.	Flux (Jy)	Distance ^a (mas)	Position angle ^a (°)	Rel. RA (mas)	Rel. DEC (mas)	FWHM (mas)	T _b (K)	UL _{T_b} ^b
2017.85	58064	A1	1.68±0.08	0.07±0.01	96.3±4.4	0.071±0.005	-0.01±0.01	0.080±0.010	2.0 × 10 ¹¹	F
		B12	0.11±0.01	0.40±0.13	6.1±4.6	0.043±0.063	0.40±0.13	0.344±0.040	7.2 × 10 ⁸	F
		A0	0.62±0.03			0.000±0.005	0.00±0.01	0.037±0.009	3.4 × 10 ¹¹	F
		B13	0.26±0.02	0.07±0.02	34.7±5.8	0.037±0.010	0.05±0.02	0.095±0.017	2.1 × 10 ¹⁰	F
2017.98	58111	B12	0.07±0.01	0.51±0.11	-0.2±3.1	-0.002±0.055	0.51±0.11	0.233±0.038	9.0 × 10 ⁸	F
		A0	1.00±0.05			0.000±0.006	0.00±0.01	0.087±0.012	9.9 × 10 ¹⁰	F
		B13	0.12±0.01	0.20±0.04	42.4±5.9	0.132±0.026	0.15±0.05	0.170±0.027	3.2 × 10 ⁹	F
2018.13	58166	B12	0.05±0.01	0.62±0.18	4.7±4.3	0.051±0.091	0.61±0.18	0.323±0.046	3.9 × 10 ⁸	F
		A0	0.70±0.04			0.000±0.005	0.00±0.01	0.020±0.006	1.3 × 10 ¹²	T
		A1	0.07±0.01	0.10±0.01	42.6±2.6	0.067±0.006	0.07±0.01	0.020±0.011	1.2 × 10 ¹¹	T
2018.19	58187	B13	0.05±0.01	0.33±0.08	38.0±6.0	0.201±0.047	0.26±0.09	0.174±0.035	1.2 × 10 ⁹	F
		B12	0.03±0.01	0.69±0.24	5.7±5.0	0.068±0.119	0.68±0.24	0.315±0.052	2.5 × 10 ⁸	F
		A0	1.53±0.08			0.000±0.005	0.00±0.01	0.036±0.007	8.8 × 10 ¹¹	F
		A1	0.04±0.01	0.17±0.01	42.2±1.6	0.116±0.006	0.13±0.01	0.020±0.012	8.3 × 10 ¹⁰	T
2018.30	58227	B13	0.04±0.01	0.40±0.13	29.6±6.6	0.196±0.070	0.35±0.14	0.208±0.041	6.1 × 10 ⁸	F
		B12	0.03±0.01	0.74±0.27	5.7±5.3	0.073±0.135	0.74±0.27	0.334±0.055	2.0 × 10 ⁸	F
		A0	2.10±0.11			0.000±0.005	0.00±0.01	0.035±0.006	1.3 × 10 ¹²	F
		A1	0.13±0.01	0.09±0.01	84.7±3.4	0.091±0.005	0.01±0.01	0.020±0.009	2.3 × 10 ¹¹	T
2018.36	58249	B13	0.04±0.01	0.43±0.09	26.3±4.1	0.189±0.049	0.38±0.10	0.153±0.036	1.1 × 10 ⁹	F
		A0	1.67±0.08			0.000±0.005	0.00±0.01	0.034±0.006	1.1 × 10 ¹²	F
		A1	0.27±0.02	0.08±0.01	70.9±4.8	0.074±0.007	0.03±0.01	0.060±0.013	5.6 × 10 ¹⁰	F
2018.45	58285	B13	0.05±0.01	0.47±0.14	24.8±5.4	0.198±0.073	0.43±0.15	0.264±0.042	5.7 × 10 ⁸	F
		A0	1.72±0.09			0.000±0.005	0.00±0.01	0.020±0.005	3.2 × 10 ¹²	T
		A1	0.13±0.01	0.11±0.02	61.7±8.8	0.096±0.018	0.05±0.04	0.124±0.023	6.2 × 10 ⁹	F
		B13	0.03±0.01	0.51±0.21	24.4±7.6	0.212±0.111	0.47±0.22	0.279±0.050	2.8 × 10 ⁸	F
2018.54	58315	A0	1.30±0.07			0.000±0.005	0.00±0.01	0.025±0.006	1.6 × 10 ¹²	F
		A1	0.07±0.01	0.12±0.03	57.2±7.6	0.100±0.018	0.07±0.04	0.095±0.023	6.1 × 10 ⁹	F
		B13	0.03±0.01	0.64±0.22	19.0±5.9	0.208±0.115	0.60±0.23	0.266±0.051	2.6 × 10 ⁸	F
2018.65	58356	A0	0.85±0.04			0.000±0.005	0.00±0.01	0.020±0.006	1.6 × 10 ¹²	T
		A1	0.82±0.04	0.02±0.01	77.8±13.9	0.021±0.005	0.00±0.01	0.024±0.006	1.1 × 10 ¹²	F
		B14	0.05±0.01	0.11±0.06	60.6±21.8	0.097±0.046	0.06±0.09	0.176±0.035	1.2 × 10 ⁹	F
2018.79	58406	A0	0.84±0.04			0.000±0.005	0.00±0.01	0.020±0.006	1.6 × 10 ¹²	T
		A1	0.82±0.04	0.05±0.01	11.1±3.3	0.009±0.005	0.05±0.01	0.049±0.009	2.5 × 10 ¹¹	F
		B14	0.11±0.01	0.11±0.06	23.4±9.6	0.043±0.030	0.10±0.06	0.177±0.029	2.6 × 10 ⁹	F
2018.94	58461	A0	1.04±0.05			0.000±0.005	0.00±0.01	0.026±0.006	1.2 × 10 ¹²	F
		A1	0.26±0.02	0.09±0.02	1.9±2.4	0.003±0.008	0.09±0.02	0.072±0.015	3.7 × 10 ¹⁰	F
		B14	0.10±0.01	0.23±0.06	2.0±3.7	0.008±0.030	0.23±0.06	0.174±0.029	2.6 × 10 ⁹	F

^a Map center is aligned to the core position^b Upper limit of T_b.

REFERENCES

- Abdo, A. A., Ackermann, M., Ajello, M., et al. 2010a, ApJ, 715, 429, doi: [10.1088/0004-637X/715/1/429](https://doi.org/10.1088/0004-637X/715/1/429)
- , 2010b, ApJ, 722, 520, doi: [10.1088/0004-637X/722/1/520](https://doi.org/10.1088/0004-637X/722/1/520)
- , 2011a, ApJ, 730, 101, doi: [10.1088/0004-637X/730/2/101](https://doi.org/10.1088/0004-637X/730/2/101)

- . 2011b, *ApJ*, 726, 43, doi: [10.1088/0004-637X/726/1/43](https://doi.org/10.1088/0004-637X/726/1/43)
- Acero, F., Ackermann, M., Ajello, M., et al. 2015, *ApJS*, 218, 23, doi: [10.1088/0067-0049/218/2/23](https://doi.org/10.1088/0067-0049/218/2/23)
- Ackermann, M., Ajello, M., Ballet, J., et al. 2012, *ApJ*, 751, 159, doi: [10.1088/0004-637X/751/2/159](https://doi.org/10.1088/0004-637X/751/2/159)
- Angel, J. R. P., & Stockman, H. S. 1980, *ARA&A*, 18, 321, doi: [10.1146/annurev.aa.18.090180.001541](https://doi.org/10.1146/annurev.aa.18.090180.001541)
- Angelakis, E., Fuhrmann, L., Myserlis, I., et al. 2019, *A&A*, 626, A60, doi: [10.1051/0004-6361/201834363](https://doi.org/10.1051/0004-6361/201834363)
- Bach, U., Krichbaum, T. P., Kraus, A., Witzel, A., & Zensus, J. A. 2006, *A&A*, 452, 83, doi: [10.1051/0004-6361:20053943](https://doi.org/10.1051/0004-6361:20053943)
- Bach, U., Krichbaum, T. P., Ros, E., et al. 2005, *A&A*, 433, 815, doi: [10.1051/0004-6361:20040388](https://doi.org/10.1051/0004-6361:20040388)
- Baring, M. G., Böttcher, M., & Summerlin, E. J. 2017, *MNRAS*, 464, 4875, doi: [10.1093/mnras/stw2344](https://doi.org/10.1093/mnras/stw2344)
- Bennett, C. L., Larson, D., Weiland, J. L., & Hinshaw, G. 2014, *ApJ*, 794, 135, doi: [10.1088/0004-637X/794/2/135](https://doi.org/10.1088/0004-637X/794/2/135)
- Berton, M., Liao, N. H., La Mura, G., et al. 2018, *A&A*, 614, A148, doi: [10.1051/0004-6361/201731625](https://doi.org/10.1051/0004-6361/201731625)
- Beuchert, T., Kadler, M., Perucho, M., et al. 2018, *A&A*, 610, A32, doi: [10.1051/0004-6361/201731952](https://doi.org/10.1051/0004-6361/201731952)
- Bhatta, G., Webb, J. R., Hollingsworth, H., et al. 2013, *A&A*, 558, A92, doi: [10.1051/0004-6361/201220236](https://doi.org/10.1051/0004-6361/201220236)
- Böttcher, M., & Baring, M. G. 2019, *ApJ*, 887, 133, doi: [10.3847/1538-4357/ab552a](https://doi.org/10.3847/1538-4357/ab552a)
- Böttcher, M., & Chiang, J. 2002, *ApJ*, 581, 127, doi: [10.1086/344155](https://doi.org/10.1086/344155)
- Böttcher, M., & Dermer, C. D. 2010, *ApJ*, 711, 445, doi: [10.1088/0004-637X/711/1/445](https://doi.org/10.1088/0004-637X/711/1/445)
- Böttcher, M., Reimer, A., Sweeney, K., & Prakash, A. 2013, *ApJ*, 768, 54, doi: [10.1088/0004-637X/768/1/54](https://doi.org/10.1088/0004-637X/768/1/54)
- Böttcher, M., Harvey, J., Joshi, M., et al. 2005, *ApJ*, 631, 169, doi: [10.1086/432609](https://doi.org/10.1086/432609)
- Butuzova, M. S. 2018, *Astronomy Reports*, 62, 654, doi: [10.1134/S1063772918100037](https://doi.org/10.1134/S1063772918100037)
- Casadio, C., Gómez, J. L., Grandi, P., et al. 2015a, *ApJ*, 808, 162, doi: [10.1088/0004-637X/808/2/162](https://doi.org/10.1088/0004-637X/808/2/162)
- Casadio, C., Gómez, J. L., Jorstad, S. G., et al. 2015b, *ApJ*, 813, 51, doi: [10.1088/0004-637X/813/1/51](https://doi.org/10.1088/0004-637X/813/1/51)
- Chen, X., Fossati, G., Liang, E. P., & Böttcher, M. 2011, *MNRAS*, 416, 2368, doi: [10.1111/j.1365-2966.2011.19215.x](https://doi.org/10.1111/j.1365-2966.2011.19215.x)
- Danforth, C. W., Nalewajko, K., France, K., & Keeney, B. A. 2013, *ApJ*, 764, 57, doi: [10.1088/0004-637X/764/1/57](https://doi.org/10.1088/0004-637X/764/1/57)
- Edelson, R. A., & Krolik, J. H. 1988, *ApJ*, 333, 646, doi: [10.1086/166773](https://doi.org/10.1086/166773)
- Emmanoulopoulos, D., McHardy, I. M., & Papadakis, I. E. 2013, *MNRAS*, 433, 907, doi: [10.1093/mnras/stt764](https://doi.org/10.1093/mnras/stt764)
- Fromm, C. M., Ros, E., Perucho, M., et al. 2013, *A&A*, 551, A32, doi: [10.1051/0004-6361/201219913](https://doi.org/10.1051/0004-6361/201219913)
- Fuhrmann, L., Larsson, S., Chiang, J., et al. 2014, *MNRAS*, 441, 1899, doi: [10.1093/mnras/stu540](https://doi.org/10.1093/mnras/stu540)
- Geng, X., Zeng, W., Rani, B., et al. 2020, *ApJ*, 904, 67, doi: [10.3847/1538-4357/abb603](https://doi.org/10.3847/1538-4357/abb603)
- Gómez, J. L., Roca-Sogorb, M., Agudo, I., Marscher, A. P., & Jorstad, S. G. 2011, *ApJ*, 733, 11, doi: [10.1088/0004-637X/733/1/11](https://doi.org/10.1088/0004-637X/733/1/11)
- Graff, P. B., Georganopoulos, M., Perlman, E. S., & Kazanas, D. 2008, *ApJ*, 689, 68, doi: [10.1086/592427](https://doi.org/10.1086/592427)
- Gurwell, M. A., Peck, A. B., Hostler, S. R., Darrah, M. R., & Katz, C. A. 2007, in *Astronomical Society of the Pacific Conference Series*, Vol. 375, From Z-Machines to ALMA: (Sub)Millimeter Spectroscopy of Galaxies, ed. A. J. Baker, J. Glenn, A. I. Harris, J. G. Mangum, & M. S. Yun, 234
- Hovatta, T., Lehto, H. J., & Tornikoski, M. 2008, *A&A*, 488, 897, doi: [10.1051/0004-6361:200810200](https://doi.org/10.1051/0004-6361:200810200)
- Hovatta, T., Tornikoski, M., Lainela, M., et al. 2007, *A&A*, 469, 899, doi: [10.1051/0004-6361:20077529](https://doi.org/10.1051/0004-6361:20077529)
- Hovatta, T., Valtaoja, E., Tornikoski, M., & Lähteenmäki, A. 2009a, *A&A*, 494, 527, doi: [10.1051/0004-6361:200811150](https://doi.org/10.1051/0004-6361:200811150)
- . 2009b, *A&A*, 494, 527, doi: [10.1051/0004-6361:200811150](https://doi.org/10.1051/0004-6361:200811150)
- Jorstad, S. G., Marscher, A. P., Mattox, J. R., et al. 2001, *ApJS*, 134, 181, doi: [10.1086/320858](https://doi.org/10.1086/320858)
- Jorstad, S. G., Marscher, A. P., Morozova, D. A., et al. 2017, *ApJ*, 846, 98, doi: [10.3847/1538-4357/aa8407](https://doi.org/10.3847/1538-4357/aa8407)
- Joshi, M., & Böttcher, M. 2011, *ApJ*, 727, 21, doi: [10.1088/0004-637X/727/1/21](https://doi.org/10.1088/0004-637X/727/1/21)
- Kadler, M., Ros, E., Perucho, M., et al. 2008, *ApJ*, 680, 867, doi: [10.1086/529539](https://doi.org/10.1086/529539)
- Karamanavis, V., Fuhrmann, L., Krichbaum, T. P., et al. 2016, *A&A*, 586, A60, doi: [10.1051/0004-6361/201527225](https://doi.org/10.1051/0004-6361/201527225)
- Kardashev, N. S., Khartov, V. V., Abramov, V. V., et al. 2013, *Astronomy Reports*, 57, 153, doi: [10.1134/S1063772913030025](https://doi.org/10.1134/S1063772913030025)
- Kim, D.-W., Trippe, S., & Kravchenko, E. V. 2020, *A&A*, 636, A62, doi: [10.1051/0004-6361/202037474](https://doi.org/10.1051/0004-6361/202037474)
- Kim, D.-W., Trippe, S., Lee, S.-S., et al. 2018, *MNRAS*, 480, 2324, doi: [10.1093/mnras/sty1993](https://doi.org/10.1093/mnras/sty1993)
- Koay, J. Y., Jauncey, D. L., Hovatta, T., et al. 2019, *MNRAS*, 489, 5365, doi: [10.1093/mnras/stz2488](https://doi.org/10.1093/mnras/stz2488)
- Kovalev, Y. Y., Kellermann, K. I., Lister, M. L., et al. 2005, *AJ*, 130, 2473, doi: [10.1086/497430](https://doi.org/10.1086/497430)
- Kovalev, Y. Y., Aller, H. D., Aller, M. F., et al. 2009, *ApJL*, 696, L17, doi: [10.1088/0004-637X/696/1/L17](https://doi.org/10.1088/0004-637X/696/1/L17)
- Kravchenko, E. V., Kovalev, Y. Y., Hovatta, T., & Ramakrishnan, V. 2016, *MNRAS*, 462, 2747, doi: [10.1093/mnras/stw1776](https://doi.org/10.1093/mnras/stw1776)
- Kravchenko, E. V., Gómez, J. L., Kovalev, Y. Y., et al. 2020, *ApJ*, 893, 68, doi: [10.3847/1538-4357/ab7dae](https://doi.org/10.3847/1538-4357/ab7dae)
- Larionov, V. M., Jorstad, S. G., Marscher, A. P., et al. 2013, *ApJ*, 768, 40, doi: [10.1088/0004-637X/768/1/40](https://doi.org/10.1088/0004-637X/768/1/40)

- Lee, J. W., Lee, S.-S., Hodgson, J. A., et al. 2017, *ApJ*, 841, 119, doi: [10.3847/1538-4357/aa72f7](https://doi.org/10.3847/1538-4357/aa72f7)
- León-Tavares, J., Valtaoja, E., Tornikoski, M., Lähteenmäki, A., & Nieppola, E. 2011, *A&A*, 532, A146, doi: [10.1051/0004-6361/201116664](https://doi.org/10.1051/0004-6361/201116664)
- Li, H., & Kusunose, M. 2000, *ApJ*, 536, 729, doi: [10.1086/308960](https://doi.org/10.1086/308960)
- Liao, N. H., Bai, J. M., Liu, H. T., et al. 2014, *ApJ*, 783, 83, doi: [10.1088/0004-637X/783/2/83](https://doi.org/10.1088/0004-637X/783/2/83)
- Liodakis, I. 2018, *A&A*, 616, A93, doi: [10.1051/0004-6361/201832766](https://doi.org/10.1051/0004-6361/201832766)
- Liodakis, I., Hovatta, T., Huppenkothen, D., et al. 2018a, *ApJ*, 866, 137, doi: [10.3847/1538-4357/aae2b7](https://doi.org/10.3847/1538-4357/aae2b7)
- Liodakis, I., Romani, R. W., Filippenko, A. V., et al. 2018b, *MNRAS*, 480, 5517, doi: [10.1093/mnras/sty2264](https://doi.org/10.1093/mnras/sty2264)
- Lisakov, M. M., Kovalev, Y. Y., Savolainen, T., Hovatta, T., & Kutkin, A. M. 2017, *MNRAS*, 468, 4478, doi: [10.1093/mnras/stx710](https://doi.org/10.1093/mnras/stx710)
- Lobanov, A. P., & Zensus, J. A. 1999, *ApJ*, 521, 509, doi: [10.1086/307555](https://doi.org/10.1086/307555)
- MAGIC Collaboration, Ahnen, M. L., Ansoldi, S., et al. 2018, *A&A*, 619, A45, doi: [10.1051/0004-6361/201832677](https://doi.org/10.1051/0004-6361/201832677)
- Mannheim, K. 1998, *Science*, 279, 684, doi: [10.1126/science.279.5351.684](https://doi.org/10.1126/science.279.5351.684)
- Marscher, A. P., Gear, W. K., & Travis, J. P. 1992, in *Variability of Blazars*, ed. E. Valtaoja & M. Valtonen, 85
- Mastichiadis, A., & Kirk, J. G. 1997, *A&A*, 320, 19, <https://arxiv.org/abs/astro-ph/9610058>
- Mattox, J. R., Bertsch, D. L., Chiang, J., et al. 1996, *ApJ*, 461, 396, doi: [10.1086/177068](https://doi.org/10.1086/177068)
- Max-Moerbeck, W., Richards, J. L., Hovatta, T., et al. 2014a, *MNRAS*, 445, 437, doi: [10.1093/mnras/stu1707](https://doi.org/10.1093/mnras/stu1707)
- Max-Moerbeck, W., Hovatta, T., Richards, J. L., et al. 2014b, *MNRAS*, 445, 428, doi: [10.1093/mnras/stu1749](https://doi.org/10.1093/mnras/stu1749)
- Nilsson, K., Pursimo, T., Sillanpää, A., Takalo, L. O., & Lindfors, E. 2008, *A&A*, 487, L29, doi: [10.1051/0004-6361:200810310](https://doi.org/10.1051/0004-6361:200810310)
- Planck Collaboration, Ade, P. A. R., Aghanim, N., et al. 2016, *A&A*, 594, A13, doi: [10.1051/0004-6361/201525830](https://doi.org/10.1051/0004-6361/201525830)
- Pushkarev, A. B., Butuzova, M. S., Kovalev, Y. Y., & Hovatta, T. 2019, *MNRAS*, 482, 2336, doi: [10.1093/mnras/sty2724](https://doi.org/10.1093/mnras/sty2724)
- Pushkarev, A. B., Hovatta, T., Kovalev, Y. Y., et al. 2012, *A&A*, 545, A113, doi: [10.1051/0004-6361/201219173](https://doi.org/10.1051/0004-6361/201219173)
- Pushkarev, A. B., Kovalev, Y. Y., & Lister, M. L. 2010, *ApJL*, 722, L7, doi: [10.1088/2041-8205/722/1/L7](https://doi.org/10.1088/2041-8205/722/1/L7)
- Pushkarev, A. B., Kovalev, Y. Y., Lister, M. L., & Savolainen, T. 2017, *MNRAS*, 468, 4992, doi: [10.1093/mnras/stx854](https://doi.org/10.1093/mnras/stx854)
- Ramakrishnan, V., Hovatta, T., Nieppola, E., et al. 2015, *MNRAS*, 452, 1280, doi: [10.1093/mnras/stv321](https://doi.org/10.1093/mnras/stv321)
- Ramakrishnan, V., León-Tavares, J., Rastorgueva-Foi, E. A., et al. 2014, *MNRAS*, 445, 1636, doi: [10.1093/mnras/stu1873](https://doi.org/10.1093/mnras/stu1873)
- Ramakrishnan, V., Hovatta, T., Tornikoski, M., et al. 2016, *MNRAS*, 456, 171, doi: [10.1093/mnras/stv2653](https://doi.org/10.1093/mnras/stv2653)
- Rani, B., Krichbaum, T. P., Marscher, A. P., et al. 2015, *A&A*, 578, A123, doi: [10.1051/0004-6361/201525608](https://doi.org/10.1051/0004-6361/201525608)
- . 2014, *A&A*, 571, L2, doi: [10.1051/0004-6361/201424796](https://doi.org/10.1051/0004-6361/201424796)
- Rani, B., Krichbaum, T. P., Fuhrmann, L., et al. 2013, *A&A*, 552, A11, doi: [10.1051/0004-6361/201321058](https://doi.org/10.1051/0004-6361/201321058)
- Richards, J. L., Max-Moerbeck, W., Pavlidou, V., et al. 2011, *ApJS*, 194, 29, doi: [10.1088/0067-0049/194/2/29](https://doi.org/10.1088/0067-0049/194/2/29)
- Robertson, D. R. S., Gallo, L. C., Zoghbi, A., & Fabian, A. C. 2015, *MNRAS*, 453, 3455, doi: [10.1093/mnras/stv1575](https://doi.org/10.1093/mnras/stv1575)
- Schinzell, F. K., Lobanov, A. P., Taylor, G. B., et al. 2012, *A&A*, 537, A70, doi: [10.1051/0004-6361/201117705](https://doi.org/10.1051/0004-6361/201117705)
- Shepherd, M. C. 1997, in *Astronomical Society of the Pacific Conference Series*, Vol. 125, *Astronomical Data Analysis Software and Systems VI*, ed. G. Hunt & H. Payne, 77
- Sikora, M., Begelman, M. C., & Rees, M. J. 1994, *ApJ*, 421, 153, doi: [10.1086/173633](https://doi.org/10.1086/173633)
- Sokolov, A., & Marscher, A. P. 2005, *ApJ*, 629, 52, doi: [10.1086/431321](https://doi.org/10.1086/431321)
- Sokolov, A., Marscher, A. P., & McHardy, I. M. 2004, *ApJ*, 613, 725, doi: [10.1086/423165](https://doi.org/10.1086/423165)
- Spada, M., Ghisellini, G., Lazzati, D., & Celotti, A. 2001, *MNRAS*, 325, 1559, doi: [10.1046/j.1365-8711.2001.04557.x](https://doi.org/10.1046/j.1365-8711.2001.04557.x)
- Teräsranta, H., Tornikoski, M., Mujunen, A., et al. 1998, *A&AS*, 132, 305, doi: [10.1051/aas:1998297](https://doi.org/10.1051/aas:1998297)
- Trippe, S., Krips, M., Piétu, V., et al. 2011, *A&A*, 533, A97, doi: [10.1051/0004-6361/201015558](https://doi.org/10.1051/0004-6361/201015558)
- Uttley, P., McHardy, I. M., & Papadakis, I. E. 2002, *MNRAS*, 332, 231, doi: [10.1046/j.1365-8711.2002.05298.x](https://doi.org/10.1046/j.1365-8711.2002.05298.x)
- Vittorini, V., Tavani, M., Paggi, A., et al. 2009, *ApJ*, 706, 1433, doi: [10.1088/0004-637X/706/2/1433](https://doi.org/10.1088/0004-637X/706/2/1433)
- Wiercholska, A., & Siejkowski, H. 2015, *MNRAS*, 452, L11, doi: [10.1093/mnras/rlv075](https://doi.org/10.1093/mnras/rlv075)
- Williamson, K. E., Jorstad, S. G., Marscher, A. P., et al. 2014, *ApJ*, 789, 135, doi: [10.1088/0004-637X/789/2/135](https://doi.org/10.1088/0004-637X/789/2/135)
- Zhang, H., Chen, X., Böttcher, M., Guo, F., & Li, H. 2015, *ApJ*, 804, 58, doi: [10.1088/0004-637X/804/1/58](https://doi.org/10.1088/0004-637X/804/1/58)